Thesis for the Degree of Doctor of Philosophy

VCSEL Equivalent Circuits and Silicon Photonics Integration

Alexander Grabowski

CHALMERS

Photonics Laboratory
Department of Microtechnology and Nanoscience
Chalmers University of Technology
Göteborg, Sweden, 2022

VCSEL Equivalent Circuits and Silicon Photonics Integration
Alexander Grabowski
©Alexander Grabowski, 2022

ISBN: 978-91-7905-681-0
Doktorsavhandlingar vid Chalmers Tekniska Högskola
Ny serie nr 5147
ISSN 0346-718X

Chalmers University of Technology
Department of Microtechnology and Nanoscience - MC2
Photonics Laboratory
SE–412 96 Göteborg
Sweden
Phone: +46–(0)31–772 10 00

Front cover illustration: Left: Equivalent circuit schematic for high-speed datacom VCSELs, with simulated eye diagram. Right: Top side micrograph of finished VCSEL with ring-type top contact, on GaAs substrate, ready for transfer-printing.

Printed in Sweden by
Chalmers Digitaltryck
Chalmers Tekniska Högskola
Göteborg, Sweden, 2022

VCSEL Equivalent Circuits and Silicon Photonics Integration

Alexander Grabowski
Photonics Laboratory
Department of Microtechnology and Nanoscience
Chalmers University of Technology

Abstract

The vertical-cavity surface-emitting laser (VCSEL) is a light source of great importance for numerous industrial and consumer products. The main application areas are datacom and sensing. The datacom industry uses GaAs-based VCSELs for optical interconnects, the short-reach fiber optical communication links used to transfer large amounts of data at high rates between units within data centers and supercomputers. In the area of sensing, VCSELs are largely used in consumer products such as smart phones (e.g. face ID and camera auto focus), computer mice, and automobiles (e.g. gesture recognition and LIDAR for autonomous driving).

In this work, an advanced physics-based equivalent circuit model for datacom VCSELs has been developed. The model lends itself to co-design and co-optimization with driver and receiver ICs, thereby enabling higher data rate transceivers with bandwidth limited VCSELs and photodiodes. The model also facilitates an understanding of how each physical process within the VCSEL affects the VCSEL static and dynamic performance. It has been applied to study the impact of carrier transport and capture on VCSEL dynamics.

The work also includes micro-transfer-printing of GaAs-based single-mode VCSELs on silicon nitride photonic integrated circuits (PICs). Such PICs are increasingly used for e.g. compact and highly functional bio-photonic sensors. Transfer printing of VCSELs enables the much-needed on-PIC integration of power efficient light sources. The bottom-emitting VCSELs are printed above grating couplers on the PIC and optical feedback is used to control the polarization for efficient coupling to the silicon nitride waveguide. Wavelength tuning, as required by the bio-sensing application, is achieved by direct current modulation.

Keywords: Vertical-cavity surface-emitting laser, optical interconnects, equivalent circuit, silicon photonics, light source integration, sensing.

List of Appended Papers

This thesis is based on the following appended papers:

[A] **A. Grabowski**, J. Gustavsson, Z. S. He and A. Larsson, "Large-Signal Equivalent Circuit for Datacom VCSELs", *IEEE/OSA Journal of Lightwave Technology*, vol. 39, no. 10, pp. 3225-3236, May 2021, doi: 10.1109/JLT.2021.3064465.

[B] **A. Grabowski**, J. Gustavsson, and A. Larsson, "Large-Signal Equivalent Circuit for Datacom VCSELs - Including Intensity Noise", Accepted for publication in *IEEE/OSA Journal of Lightwave Technology*, doi: 10.1109/JLT.2022.3200905.

[C] **A. Grabowski**, J. Gustavsson, and A. Larsson, "Impact of Carrier Transport and Capture on VCSEL Dynamics", Submitted to *IEEE Journal of Quantum Electronics*.

[D] J. Goyvaerts, **A. Grabowski**, J. Gustavsson, S. Kumari, A. Stassen, R. Baets, A. Larsson, and G. Roelkens, "Enabling VCSEL-on-silicon nitride photonic integrated circuits with micro-transfer-printing", *Optica*, vol. 8, no. 12, pp. 1573-1580, Dec 2021, doi:10.1364/OPTICA.441636.

Related publications and conference contributions by the author not included in this thesis:

Journal paper

[E] S. Giannakopoulos, I. Sourikopoulos, L. Stampoulidis, P. Ostrovskyy, F. Teply, K. Tittelbach-Helmrich, G. Panic, G. Fischer, **A. Grabowski**, H. Zirath, P. Ayzac, N. Venet, A. Maho, M. Sotom, S. Jones, G. Wood, I. Oxtoby "A 112 Gb/s Radiation-Hardened Mid-Board Optical Transceiver in 130-nm SiGe BiCMOS for Intra-Satellite Links", *Frontiers in Physics*, vol. 9, 672941, May 2021. doi:10.3389/fphy.2021.672941.

Conference contribution

[F] **A. Grabowski**, J. Gustavsson, Z. S. He and A. Larsson, "Large-Signal Circuit Model for Datacom VCSELs", *2018 IEEE International Semiconductor Laser Conference (ISLC)*, 2018, pp. 1-2, doi: 10.1109/ISLC.2018.8516232.

Unpublished conference contributions

[G] **A. Grabowski**, J. Gustavsson, Z. S. He and A. Larsson, "Large-Signal Circuit Model for Datacom VCSELs", *VCSEL Day 2018*, 2018.

[H] **A. Grabowski**, J. Gustavsson, Z. S. He and A. Larsson, "Large-Signal Circuit Model for Datacom VCSELs", *Photonics West 2020*, 2020.

Contents

Acknowledgement

First and foremost, I would like to express my large gratitude to both my supervisors and my examiner. My previous main supervisor, now co-supervisor, Dr. Johan Gustavsson, for immense support, very interesting discussions and excellent guidance. I would also like to thank my examiner and supervisor Prof. Anders Larsson, for all his support and for giving me the opportunity to work in this more-than-fantastic lab and produce this thesis and the results behind it.

Then, there are several people that cannot go unmentioned. Dr. Erik Haglund for being my co-supervisor and supporting me, both during my master's thesis and the beginning of my PhD studies. Both Dr. Ewa Simpanen and Dr. Emanuel P. Haglund for teaching me about VCSEL fabrication and providing aid in the measurement lab. Dr. Tamás Lengyel for providing aid in measurements. Dr. Mehdi Jahed for fruitful discussions regarding cleanroom fabrication, life and being my fantastic office mate for a long time.

Furthermore, I would like to acknowledge all of our excellent external collaborators at the Photonics Research Group in Ghent University-imec. Special thanks to Dr. Jeroen Goyvaerts for working tirelessly together on the micro-transfer-printing of VCSELs on SiNx PICs. Also thank you to Prof. Günther Roelkens and Prof. Roel Baets, for the expertise provided in this project.

Thank you to Dr. Stavros Giannakopoulos, Dr. Attila Fülöp, Dr. Michael Alexander Bergmann, Dr. Filip Hjort, Dr. Lars Lundberg, Hans Kaimre, Erik Strandberg for lighting up the lab and both the scientific and non-scientific discussions. Another thank you to Dr. Óskar Bjarki Helgason, whom I have known and studied along side with since my master's programme at Chalmers, thanks for everything, especially for all the quirky discussions.

Thank you to everyone unmentioned above, at the Photonics Laboratory, for keeping spirits up, and making this a great work place, and

always providing an opportunity for discussions.

A big thank you also goes out to our administrators Gunnel Berggren and Jeanette Träff, for making our lives easier and always helping out with tricky bureaucracy.

I also would like to thank the Nanofabrication Laboratory staff for fantastic support and keeping the cleanroom tools working.

An enormous thank you to all my friends, for making life more fun and for all your friendships.

Last, but certainly not least, I would like to thank my parents, Arkadiusz and Małgorzata, and the rest of my family; for your immense support and love throughout my studies, and life. I would not be here if it was not for you.

This work is financially supported by the Swedish Foundation for Strategic Research (project Hot-Optics, CHI19-0004), the Swedish Foundation for Strategic Research (project MuTOI, SE13-0014), and the European Union's Horizon 2020 Research and Innovation Program (project PIX4life, 688519). IQE Europe and JENOPTIK AG are acknowledged for supplying the epitaxial VCSEL materials. This work was performed in part at Myfab Chalmers.

May the Force be with you,
Alexander Grabowski

Göteborg
September 2022

List of Abbreviations

APC	angled physical contact
AR	anti-reflection
ASIC	application-specific integrated circuit
AWG	arbitrary waveform generator
BCB	benzocyclobutene
BER	bit-error-ratio
BPG	bit pattern generator
CCD	charged-coupled device
CMOS	complementary metal-oxide-semiconductor
CW	continuous-wave
DBR	distributed Bragg reflector
DC	direct current
DSP	digital signal processing
DVS-BCB	divinylsiloxane benzocyclobutene
EA	error analyzer
EEL	edge emitting laser
ESA	electrical spectrum analyzer
FEC	forward-error-correction
FP	Fabry-Pérot
FWHM	full-width at half-maximum
GC	grating coupler
IBE	ion beam etching
IC	integrated circuit
ICP	inductively-coupled plasma
IR	infrared
LIDAR	light detection and ranging
LP	linearly polarized
MM	multi-mode
MOCVD	metal-organic chemical-vapor deposition

OI	optical interconnect
OOK	on-off keying
OSA	optical spectrum analyzer
PAM4	4-level pulse-amplitude-modulation
PD	photodiode
PDMS	polydimethylsiloxane
PECVD	plasma-enhanced chemical vapor deposition
PIC	photonic integrated circuit
QW	quantum well
RF	radio frequency
RIE	reactive-ion etch
RIN	relative intensity noise
RMS	root-mean-square
RT	room temperature
SCH	separate confinement heterostructure
SiN	silicon nitride
SiNx	silicon nitride
Si_3N_4	silicon nitride
SiP	silicon photonics
SiPh	silicon photonics
SM	single-mode
SMSR	side-mode suppression ratio
SNR	signal-to-noise ratio
SOI	silicon-on-insulator
TE	transverse electric
TM	transverse magnetic
UV	ultraviolet
VCSEL	vertical-cavity surface-emitting laser
VNA	vector network analyzer
VOA	variable optical attenuator
WG	waveguide

Chapter 1

Introduction

According to the Cisco VNI for 2017-2022 [1], in the year 2017, 1.5 zettabytes (ZB) of IP-traffic was transmitted over the Internet, with projections of 4.8 ZB for 2022. To put this into a more everyday perspective, a zettabyte is a billion terabytes. Projections up to 2030 show an even larger, exponential, growth of data transmitted globally, with mobile data becoming increasingly more popular [2].

This increase is not only driven by the rise in number Internet users, which is dominated by low income countries [3], but also by a general demand for faster data transfer speeds [4] caused by higher definition video streaming such as 4K and 8K video, cloud storage and computing etc. More devices connected to the Internet is also a factor.

1.1 VCSELs for Optical Interconnects

Whether we are watching YouTube, sending a message through Facebook, using Dropbox or hosting a website on Amazon's AWS, something has to process the information necessary for the users. This backbone of the Internet is data centers. These are large facilities with areas of up to hundreds of football fields. The currently largest data center [5] spans an area of 140 FIFA recommended football fields, has 6 data halls, and requires roughly the same electrical power, 150 MW, as is provided by a small modular nuclear reactor [6].

In data centers, various computing, switching and storage units are are stacked in racks, and in turn in rows/pods and interconnected using primarily fiber optical and copper cable connections. Copper cables are mainly utilized for very short distances. Short reach optical links

are known as optical interconnects (OIs). An optical interconnect consists of an optical transmitter, an optical fiber, and an optical receiver. Since the communication is bi-directional, transmitters and receivers are combined in transceivers. On the transmit-side, a semiconductor laser connected to an electric driver integrated circuit (IC) is used to generate the optical signal. On the receive-side, a photodiode (PD) connected to a transimpedance amplifier detects and amplifies the signal. OIs are not only used in data centers, but also in high-performance computing applications (also known as supercomputers). Of all the traffic inside a data center, only 15% is sent back to the users, and 71% stays within the data center, while the remaining 14% is sent between data centers [7], meaning that the traffic load is heavily dominated by relatively short datacom links.

As data centers transfer this tremendous amount of data, and since optical networking consumes a substantial amount of power, the OIs have to be, apart from reliable: cost-efficient, energy-efficient and capable of providing high-speed data transfer. This is the reason why a semiconductor laser referred to as a vertical-cavity surface-emitting laser (VCSEL) is employed for this purpose, capable of sub-pJ-order of energy consumption per bit per laser at rates of tens of Gigabits per second [8]. These OIs are heavily dominated by multi-mode (MM) 850 nm wavelength GaAs-based VCSELs for reaches below 300 m [9].

The transmitter part of an OI consists of a driver circuit, which translates digital bits to an analog signal, which electrically drives the VCSEL that converts it to intensity modulated light. The light from the VCSEL is coupled into a MM-fiber, and sent to the receiver end of the OI. Here a photodiode (PD) converts the incoming light into an electrical signal, which is then amplified and converted back into digital bits.

Despite 850 nm GaAs VCSELs heavily dominating the datacom market for shorter-reach OIs, high-speed VCSELs in the ranges of 1.3 μm and 1.55 μm for both data- and telecom also exist, and are predominantly InP-based [10]. These can potentially be used in data centers for longer reach links than GaAs-VCSELs, since at these wavelengths the optical fiber has minimum chromatic dispersion and attenuation, respectively.

1.2 VCSELs for Sensing

Apart from communication applications, VCSELs are heavily employed in sensing applications. As consumer products become increasingly more

functional, ranging from self-driving cars to smartwatches, they require more sophisticated electronics and photonics. Sensors are important in most products, and since VCSELs are energy-efficient and can provide good beam characteristics due to their circular symmetry and techniques for transverse mode and polarization control, they are heavily used in optical sensing applications, where these features are key aspects [9].

Among the large volume applications areas of VCSEL sensors among consumer products are smartphones. Several different types of VCSEL-based sensors are present in a smartphone. For example, the proximity sensor which measures the distance to your head, and turns off your screen during phone calls [11]. Next, the camera auto focus in smartphones is typically VCSEL-based [11]. In Apple's Face ID, a VCSEL array is used together with a diffractive optical element to create a dot-matrix on the user's face [12].

Autonomous vehicles is a large upcoming market for sensing-VCSELs, as the vehicles require a tremendous amount of sensors to scan the environment, using among others LIDAR ("light-based RADAR"). These are typically based on high power VCSEL arrays [13].

Finally, the application of VCSELs for biosensing should not go unmentioned, as this is the main aim of Paper D. Such applications can for example involve sensors to detect concentrations of salts in sweat using smartwatches.

1.3 Outline of This Thesis

This thesis is divided into 8 Chapters. The thesis introduction can be found right above, here in Chapter 1. The thesis continues by introducing the basics of VCSELs in Chapter 2, and dives more into the dynamics of the VCSEL in Chapter 3. Chapter 4 deals with modelling of VCSELs, which is related to Papers A-C. Further, Chapter 5 provides an introduction to integration of VCSELs on silicon-based photonic integrated circuits (PICs), while Chapters 6 presents the fabrication of VCSELs for such integration, both of which are related to Paper D. An outlook on the topics are given in Chapter 7. The thesis is concluded in Chapter 8 with a summary of the appended papers. The appended papers can be found in the back of the thesis, right after the references.

Chapter 2

Vertical-Cavity Surface-Emitting Lasers

2.1 Background and Basics

The fundamental physical process behind lasing is stimulated emission, which was already in 1917 predicted by Albert Einstein [14]. The two other radiative processes are the (stimulated) absorption and spontaneous emission processes. In the case of an atom, during absorption an electron absorbs the energy from a photon which excites the electron to a higher energy level, while spontaneous emission means an already energy-excited electron relaxes spontaneously and emits a photon with energy corresponding to the energy lost. The process behind lasers, stimulated emission, occurs during the interaction of an energetically excited medium and an incoming photon, and creates a copy of the photon, with the same frequency, polarization and propagation direction, while de-exciting. For a semiconductor material used in lasers, which does not work based on discrete electron energy levels like in an atom but rather on bands of states, a forward bias voltage is applied to a *pn*-junction. This leads to free carrier injection and accumulation of excess electrons in the conduction band and holes in the valence band which creates the population inversion needed for net stimulated emission and optical gain.

The basic principle behind a laser involves several elements and processes [15], all of which are important.

- Gain medium - A material that amplifies light through means of stimulated emission

- Energy - To pump/invert the gain medium, usually electrically or optically
- Optical feedback - Most commonly some type of mirrors, which form an optical resonator
- Optical leakage - Some light must leak out of the resonator, otherwise no useful light would be emitted

Some photons will be created by spontaneous emission, and the ones with optimal properties such as wavelength and direction will repeatedly bounce between the mirrors, being copied multiple times with each round-trip until a steady-state condition is reached where the gain balances the losses. Figure 2.1 shows a schematic of a simple mirror-based laser design.

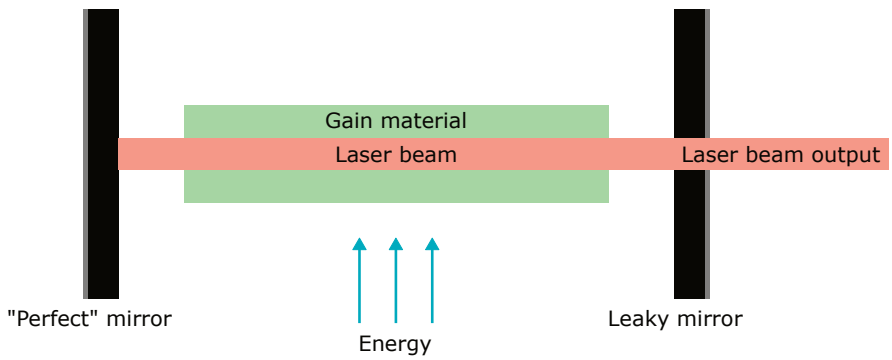

Figure 2.1: A schematic figure of a simple laser design, a pumped gain medium in-between two mirrors, one of which is fully reflective and one which leaks light.

In order to achieve lasing, the gain medium in a semiconductor laser (e.g. VCSEL) has to be pumped to the threshold material gain, where the gain and the resonator losses are equal. This threshold gain can be expressed as

$$g_{th} = \frac{1}{\Gamma}\left(\alpha_i + \alpha_m\right) = \frac{1}{\Gamma}\left(\alpha_i + \frac{1}{2L}\ln\left(\frac{1}{R_1 R_2}\right)\right), \tag{2.1}$$

where Γ is the confinement factor, a measure of the overlap of the optical field and the gain region, L is the cavity length and α_i and α_m are the internal and mirror losses, respectively.

There is also a second condition for a laser to work properly, which is the phase condition

$$\exp\left(-j\frac{2\pi}{\lambda_0}2Ln_{eff}\right) = 1, \tag{2.2}$$

where n_{eff} is the effective refractive index of the cavity, and λ_0 is the lasing wavelength in vacuum. This expression is fulfilled when

$$\lambda_0 = \frac{2Ln_{eff}}{m}, \tag{2.3}$$

where m is a non-zero integer. This means that the condition is "cyclic" and there exists several wavelengths that are supported by the resonator, these are the longitudinal modes [16]. However, most of them will be unable to lase because they will fall outside of the gain spectrum of the active region or the reflectivity spectrum of the mirrors. For a VCSEL, typically only one longitudinal mode is supported, due to L being very small.

2.2 Some History

While a laser is considered a device, the term originally stems from the acronym "light amplification by stimulated emission of radiation", which describes the physical principle of optical gain. The first demonstration of a laser happened in year 1960, by Theodore Maiman, who used a flash lamp to excite a ruby crystal [17]. Since this invention 62 years ago, tremendous strides have taken place in this field. Lasers with the size of a few nanometers such as the spaser [18], to lasers which are larger than a football field and employed for fusion research have been invented since [19]. Lasers also function based on gain technologies from gases such as He-Ne [20] to electrical injection of semiconductor materials [21, 22], while crystal-based lasers such as the very popular Nd:YAG [23] are also still employed.

The VCSEL was first proposed by Kenichi Iga in 1977 [24], and demonstrated at the relatively low temperature of 77 K two years later, in 1979 by Soda, Iga, Kitahara and Suematsu [25]. The very important milestone of continuous-wave (CW) operation at room temperature (RT), was first achieved in 1988 [26] and the details were later published in 1989 [27]. Since then, VCSELs have become a dominating choice for

applications in optical interconnects [9] and various sensors, e.g. computer mice [28], LIDARs (light detection and ranging, essentially an optical radar) [29], smartphone camera auto focus [30] and face ID [12].

2.3 VCSEL Structure and Basic Concepts

The vertical-cavity surface-emitting laser (VCSEL) is a semiconductor based laser which, as the name indicates, has its resonator aligned in the vertical direction. The light is most commonly emitted through the top mirror, however bottom-emitting VCSELs are also relatively common. As already stated in the introduction, this thesis concentrates on GaAs-based 850 nm VCSELs, however, much of the knowledge presented here can be transferred to conventional GaAs-based VCSELs with longer wavelengths, up to around 1100 nm [31], and shorter wavelengths, down to around 630 nm [32].

VCSELs consist of an undoped active region placed between two higher bandgap distributed Bragg reflector-based (DBR) mirrors with very high reflectivity. Usually the mirrors are *p*- and *n*-doped, and create a *pn*-junction that is forward biased to achieve optical gain in the active region through current injection. Electrical current injection is achieved using *p*- and *n*-contacts and gold based contact pads for ease of probing.

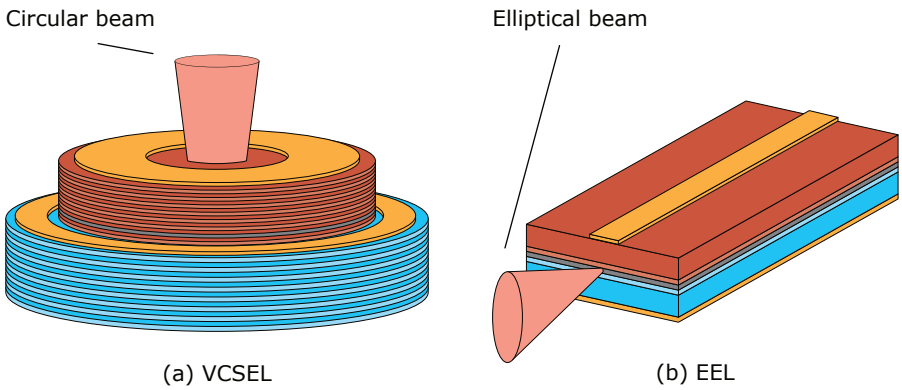

Figure 2.2: Three dimensional side by side comparison of a VCSEL (a) and an EEL (b).

Comparing the VCSEL to one of the most simple and common semiconductor laser types, the edge-emitting laser (EEL) (first prototype demonstrated in 1962 [33]) also called Fabry Pérot-laser, or FP-laser for

short, highlights quite a few geometrical differences. Figure 2.2 shows both lasers side by side. Contrary to the VCSEL's vertical light output, the EEL is emitting its light through its sides, and the resonator is formed in the horizontal direction, which is typically created by cleaving the material in a careful fashion. This means that the EEL cannot be tested on wafer during fabrication, as the last step enables the lasing through creation of the reflective facets. A VCSEL, however, can be tested already during fabrication, on the wafer. This provides a distinct fabrication advantage, and together with its small volume, VCSELs can be fabricated in a high-yield and cost-efficient manner. Also, the VCSEL has a circular beam while the EEL has, due to its asymmetric waveguide design, an elliptical output beam, which makes lens coupling into fibers more troublesome than with a circular one. However, due to its small volume the VCSEL suffers from performance decrement due to thermal effects at lower injection currents than the EEL.

Figure 2.3 shows a cross-section of a simple (low-speed) VCSEL, together with the standing optical wave in the vertical z-direction. The details will be explained in the upcoming Sections.

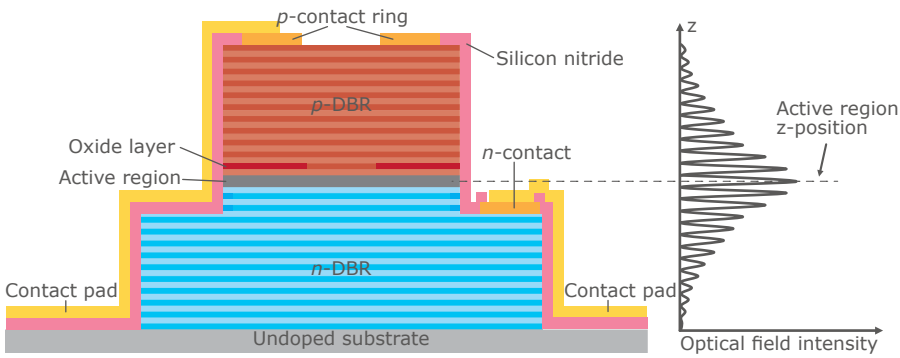

Figure 2.3: Cross-sectional schematic of a simple top emitting p-side up VCSEL, with oxide confinement and intra-DBR n-contact, with the standing optical wave supported by the vertical resonator shown side-by-side.

2.4 Mirrors and Resonator

The mirrors of a VCSEL are referred to as distributed Bragg reflectors (DBRs), which are quarter-wavelength thin slabs of either epitaxial

(GaAs-based) or dielectric materials of alternating high and low index materials.

In the case of GaAs-based VCSELs, dielectric mirrors are sometimes used with half-VCSELs, where the dielectric DBR is added at a later processing stage, and can be made of for example SiO_2/TiO_2 [34]. The epitaxial mirrors in GaAs VCSELs are almost exclusively made of $Al_xGa_{1-x}As$ with the two different slabs having low and high aluminum concentrations, for example 12% and 90% [35], and often with graded Al-concentration transitions instead of sharp ones to easy carrier transport. Apart from good electrical and thermal conductivity, an added benefit of using this material system is the lattice compatibility with GaAs, as the lattice constants of low- and high-aluminum $Al_xGa_{1-x}As$ are close [36].

The active region of a VCSEL is usually very thin (small gain per round-trip), and thus the mirrors must be highly reflective (>99%) to provide a high number of round-trips for the light. Because of relatively low refractive index contrast in the AlGaAs-system, the number of slab pairs in the DBRs is high, in the order of tens of pairs, typically around 20-30 [37]. Figure 2.4 shows an example of a top side power reflectivity spectrum for a simple 850 nm VCSEL, which is pumped to transparency meaning zero gain. While it is important to have a matching DBR with quarter-wavelength thick slabs, the wavelength is primarily set by the length of the cavity (distance between DBRs) and the closest DBR-pairs as the optical wave interacts more with those than the outer DBR-pairs.

2.5 Active Region - Optical Gain and Spontaneous Emission

The VCSEL active region, placed in the cavity (between the DBRs), is based on multiple quantum wells (QWs) in order to provide gain through stimulated emission. For modern 850 nm GaAs VCSELs, QWs are typically composed of either GaAs or InGaAs, where InGaAs is used in designs where a high modulation bandwidth is required, as this provides a strained structure which increases differential gain [38]. For these high-speed designs, predominantly 3 to 5 QWs are used, as adding more QWs will lead to QWs that do not overlap with the optical wave well enough to be considered beneficial. The thickness of the cavity is a half-integer wavelength (1/2-λ, 1-λ, 3/2-λ etc.), but most commonly uses 1/2-λ or 3/2-λ thickness.

The QWs are located next to each other inside the higher bandgap

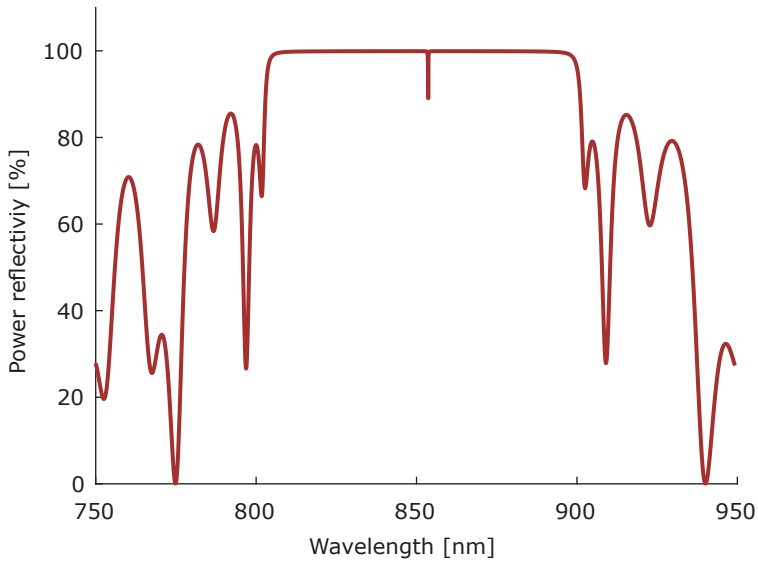

Figure 2.4: Power reflectivity spectrum for a 850 nm VCSEL, pumped to transparency.

separate confinement heterostructure (SCH), with AlGaAs barriers in-between, which efficiently traps carriers and with sufficient electrical injection provides high carrier densities. For an overview of this active area, see Figure 2 in Paper A. The number of QWs needs to be chosen keeping in mind that the overlap with the standing optical wave and the combined material gain of the QWs are both relevant factors [39], and that the differential gain (Section 3.1) is affected by the number and thickness of the QWs since it depends on the carrier density [40]. The QWs are typically a few nanometers thick.

The QWs do not only provide gain through stimulated emission, but also emit light through spontaneous emission, a process first presented by Dirac in 1927 [41]. The carriers bound inside the QWs can recombine spontaneously and emit photons with a random direction, polarization, and with a broader spectrum than in the case of stimulated emission. However, there are also non-radiative spontaneous recombination processes. The total rate of all spontaneous recombination processes is typically explained using three recombination coefficients, the

Shockley-Read-Hall-recombination coefficient A, the radiative recombination coefficient B and the Auger recombination coefficient C. The recombination rate can be expressed as [42]

$$R_{sp}(N) = A \cdot N + B \cdot N^2 + C \cdot N^3, \tag{2.4}$$

where N is the density of excess free carriers (holes and electrons), assuming an equal number of each excess carrier. The Shockley-Read-Hall and Auger recombinations are both of the non-radiative type and are related to defects and excess energy free carrier collisions [42], respectively. The radiative recombination is as the name would suggest the process which generates photons through spontaneous emission, and a small portion of this light is coupled into the resonator modes, while most is lost.

2.6 Electro-optical Confinement Methods

While the light inside the VCSEL is confined in the longitudinal (vertical) direction by the DBRs, it must also be confined in the transverse (horizontal x-y-plane) direction. Therefore, the processing of VCSELs must take this into account. The same goes for the pumping. Modern GaAs-based VCSELs are usually electrically injected in the vertical direction, see Figure 2.3, between the p- and n-contacts. Optimally, all the injected carriers should be confined to the transverse area of the active region where the optical modes are present.

A few methods for doing this for GaAs VCSELs are shown in Figure 2.5. The simplest one is etching an air post around the top mesa [43]. While this is very simple, it is also largely inefficient due to lower thermal conductivity from the surrounding air and large scattering losses at the mesa-air interfaces. A method taking the etched air post a step further is regrowth. Regrowing the surroundings with a semi-insulating semiconductor minimizes the cons discussed for the etched air post approach. However, the regrowth processes is difficult to perform on the AlGaAs-materials. Another issue with both these methods is the contact ring geometry, which is hard to design and deposit without it interacting with the beam and causing unwanted reflections and further losses. Proton implantation is another method to provide confinement [44], as the implanted protons confine the current very well in the transverse direction. However, proton implantation does not provide any optical confinement as it does not affect the refractive index to enough extent.

This makes the optical beam characteristics entirely dependent on effects such as contact ring geometry, spatial hole burning, and also thermal lensing [45]. The implantation is done by accelerating and physically pushing protons inside the material, which increases the resistivity. Neither of these techniques are used in Papers A–D appended in this thesis.

The last type of confinement shown in Figure 2.5 is using selective oxidation [46], which forms an oxide aperture in the VCSEL. This is done by oxidizing high-aluminum AlGaAs (Papers A–D: $Al_{0.98}Ga_{0.02}As$) using hot water vapour at high temperature (420°C in our cleanroom setup). This step is done after etching of the top mesa. The layer is electrically isolating, thus it confines the current to the aperture. The oxidized part of the layer has a lower refractive index, and can thus guide light. The optical guiding and confinement is affected by the size of the oxide aperture as this plays a major role for the number of modes capable of lasing. The thickness and vertical placement of the oxide layer(s) is important because of the overlap with the optical field, placing it at a field maxima will make the oxide layer guide the modes more strongly but also introduces more scattering losses, and vice versa [47].

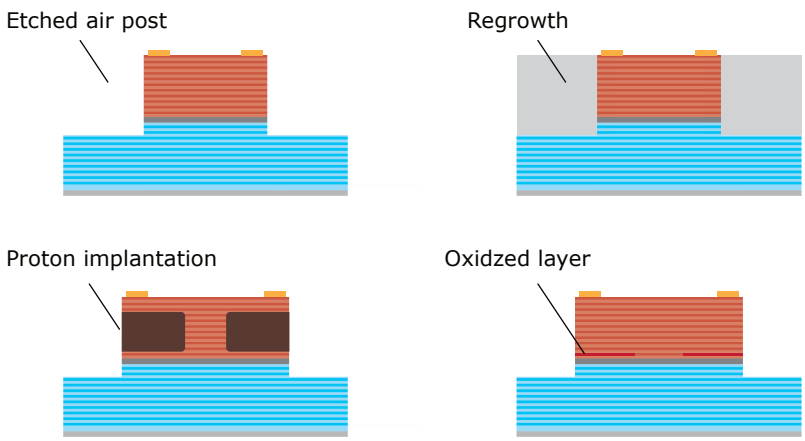

Figure 2.5: Various methods for confining the injection current and the optical modes in the transverse direction inside a VCSEL.

2.7 Thermal Properties

The gain spectrum red-shifts with temperature, this rate is dependent on several factors, among which the most important ones are QW composition and thickness. The rate at which the gain peak shifts is 0.32-0.33 nm/K [48]. However, the gain spectrum does not set the resonance wavelength. As mentioned earlier, this is done by the VCSEL cavity, which is mainly controlled by the effective optical thickness of the cavity, but the thicknesses of the DBR-layers have to match this in order to provide sufficient reflectivity at the resonance wavelength. Mainly due to resistive Joule heating under current injection, the materials from which the VCSEL is made of heat up, and the effective optical length of the cavity changes due to the temperature dependence of the refractive indices. Thermal expansion also plays a role, but is a rather negligible effect in comparison to the refractive index variations. The change of the optical length of the cavity with temperature therefore red-shifts the resonance wavelength, at a rate of roughly 0.06-0.09 nm/K [49], depending on VCSEL composition.

Figure 2.6 shows the principle of the shift of the resonance wavelength and the gain spectrum with temperature, one can see that the modal gain will vary with temperature based on the overlap of the resonance wavelength and the gain spectrum, which changes with temperature. At RT, the difference in wavelength between the resonance wavelength and the peak of the gain spectrum is commonly referred to as ”detuning”.

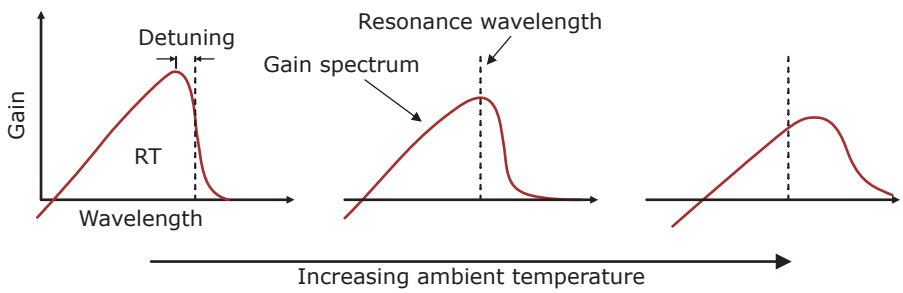

Figure 2.6: Schematic illustrating how gain spectrum and resonance wavelength overlap changes with temperature.

2.8 Modal, Spectral and Polarization Characteristics

While VCSELs only support a single longitudinal mode (within the gain spectrum) that fulfills Equation 2.3, the geometry of the device may allow for several transverse modes (lateral direction), depending mostly on the diameter of the optical confinement. VCSELs with a smaller confinement diameter will have fewer modes than the ones with larger confinement diameter (e.g. oxide aperture).

The transverse modes that can resonate in the VCSEL are solutions to the Helmholtz wave equation in the VCSEL resonator. In a circular-symmetric geometry such as this, these modes are referred to as Laguerre-Gaussian modes [50], which is a special case of the Ince-Gaussian modes which can exist in elliptical geometries [51]. The modes are commonly named LP modes, which stands for linearly polarized modes, and is not only used in the context of VCSELs but all radially symmetric devices, including optical fibers. Figure 2.7 shows a cross-sectional representation (in the x-y-plane) of the LP mode intensities, where the fundamental Gaussian mode is denoted LP_{01} and the higher order modes LP_{lm} where l and m are positive integers. The complex amplitude at the waist ($z = 0$) of these modes can be described as [16]

$$U_{lm}(r,\phi) = A_{lm}\left(\frac{r}{\omega_0}\right)^{l} L^{l}_{(m-1)}\left(\frac{2r^2}{\omega_0^2}\right)\exp\left(\frac{r^2}{\omega_0^2}\right)\exp\left(-jl\phi\right). \quad (2.5)$$

Here, l is the number of the generalized Laguerre polynomial function $L^{l}_{(m-1)}$ and $(m-1)$ the order of that polynomial. Further, r and ϕ denote the radius and azimuthal angle, and ω_0 the $1/e^2$ radius, while A_{lm} is the amplitude factor. The presence of the phase factor $\exp(-jl\phi)$ in Equation 2.5 means that the intensity profiles of the modes with $l > 0$ (any modes with an azimuthal dependence) will have two 90° relatively rotated states.

The most confined mode, the fundamental Gaussian mode, experiences the highest effective refractive index, since it has least interaction with the surrounding lower refractive index guide of all the modes, and has therefore the longest wavelength, since the optical path is determined by multiplying the physical path with the effective refractive index. With higher mode order, the wavelength decreases. Figure 2.8 shows a spectral measurement of two different VCSELs, where the upper two Subfigures

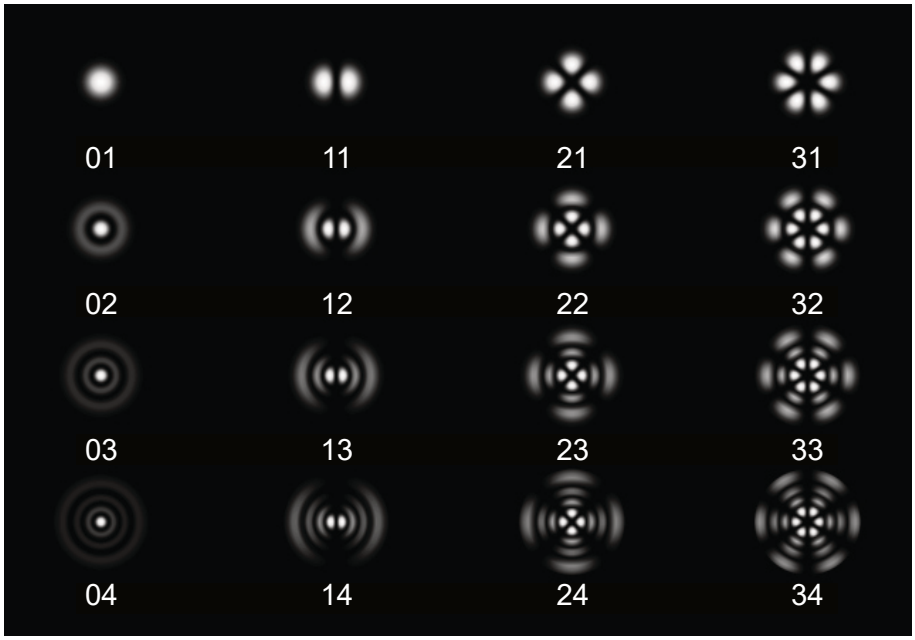

Figure 2.7: Intensity of different LP_{lm} modes that can potentially resonate inside a VCSEL [52].

in red are for a single-mode (SM) VCSEL and the lower two in purple for a multi-mode (MM) VCSEL. For each Subfigure, the bias current is also indicated, showing for both cases how the modes move because of current-induced heating, by refractive index change in the cavity, but also for the MM case how the modal characteristics can change with current. This leads to a very distinct spectral width increment for a MM VCSEL compared to a SM VCSEL. The current-induced wavelength red-shift can be taken advantage of and used for wavelength-tuning, as done in Paper D.

The transverse modes also have polarization states, each mode with two orthogonal polarization states denoted TE and TM. TE stands for transverse electric and TM stands for transverse magnetic. In a TE-polarization state the electric field of the electromagnetic wave oscillates in a direction orthogonal to the direction of propagation, whereas the TM-polarization has its magnetic field in a direction orthogonal to the direction of propagation [16]. This effectively means that all modes with $l = 0$ have two states with orthogonal polarization, and all of the modes with $l > 0$ have four states (two rotational states, each with two polar-

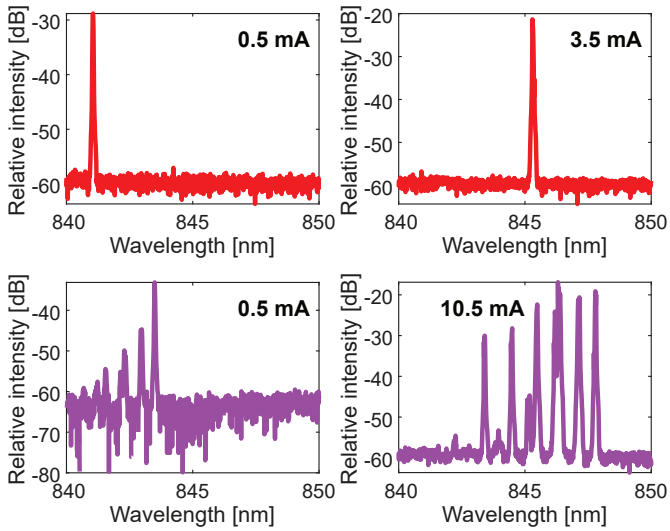

Figure 2.8: Spectra for SM VCSEL (upper two Subfigures, red) and MM VCSEL (lower two Subfigures, purple), for various bias currents.

ization states).

2.9 VCSEL Static Measurements and Performance

2.9.1 Measurement Setups

There are several important static performance measures of a VCSEL. The most basic measurement is the IPV, also called LIV, where I stands for current, P for (optical) power, V for voltage and L for light (light = optical power). This measurement is performed by sweeping the bias current of the VCSEL and for each current measuring the voltage applied to the VCSEL and the optical output power. The voltage is typically measured using a voltage meter. Measuring the optical power is slightly more tricky, and there is a wide array of options for doing this. The easiest one is catching the light using a large area photodiode (PD) and measuring the generated photocurrent, usually through a load resistor and voltage meter. Another, more accurate, method of measuring the optical power from the VCSEL is using an integrating sphere. An integrating sphere [53] uses a detector specially calibrated for it, and makes use of highly reflective surfaces inside it, that scatter light in all direc-

tions, creating an almost isotropic light profile inside, for which a non-line of sight detector inside is calibrated. This method is an indirect light measurement, but typically a more accurate one than simply using a PD, as the PD might either not catch all light due to beam divergence or not accept all light due to reflections.

The ambient temperature of the VCSEL is controlled using a Peltier element connected to a metal chuck upon which the VCSEL-chip is placed, and a temperature controller.

Measuring the VCSEL optical spectrum is another, this is typically done using an optical spectrum analyzer (OSA). The light from the VCSEL has to be coupled into a fiber, which connects to the OSA. The OSA sweeps the wavelength using a narrow filter ($<<1$ nm) and measures the power at each point, see Figure 2.8 for an example. The coupling to the fiber can be done in a couple of different ways. The simplest is to cleave the fiber and hover it over the output of the VCSEL. The fiber can also be lensed. Another option is to combine a fiber with an anti-reflection (AR)-coated lens system to maximize coupling and minimize optical feedback by tilting the fiber.

2.9.2 Performance Measures

Figure 2.9 shows an IPV measurement with a few important performance measures marked:

- Threshold current: A low threshold current typically implicates a resonator with low losses, and vice versa. But low losses can be a drawback, since this means that the total losses are low, including the mirror losses, which means that there is little light coupled out and the output power and slope efficiency are low.

- Slope efficiency: Measured in Watts per Ampere, and relates the increase of output power to the increase of input current above threshold.

- Roll-over: The roll-over (current) is typically indicative of the thermal characteristics of the laser. A lower roll-over current means more heat is generated and/or not dissipated away from the VCSEL quickly enough (high thermal impedance).

- Differential resistance: Measured in Ohms (or Volts per Ampere), is the slope of the IV-curve, but is non-linear so the VCSEL's

differential resistance changes with current. Essentially the lower the better, since this means less heat generation.

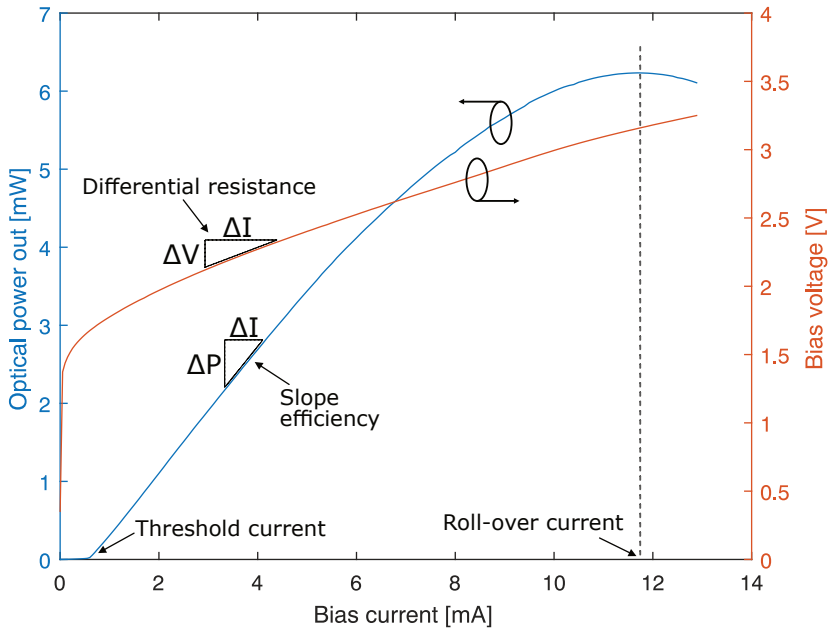

Figure 2.9: IPV plot with some important performance measures marked.

A sometimes important performance measure of the spectral measurement is the side mode suppression ratio (SMSR), which determines whether a VCSEL is single-mode or multi-mode (or quasi-single-mode). There is no strict definition of single-mode operation, but typically 30-40 dB suppression of higher order transverse modes is required, depending on application.

Another spectral performance measure is the root-mean-square (RMS) spectral width. This is a measure employed for MM VCSELs, due to broadening of the spectrum caused by the fact that different transverse modes lase at slightly different wavelengths (see Figure 2.8). The RMS spectral width is defined as [54]

$$\Delta\lambda_{RMS} = \sqrt{\sum_{i=1}^{n} \frac{P_i}{P_{tot}} (\lambda_i - \lambda_{mean})^2}, \quad \text{where} \quad \lambda_{mean} = \sum_{i=1}^{n} \frac{P_i}{P_{tot}} \lambda_i, \tag{2.6}$$

where P_i and λ_i are the power and wavelength at point i in the measured spectrum, P_{tot} is the total power and λ_{mean} is the average wavelength of the measurement. For SM VCSELs however, the term linewidth is more commonly used, as only a single mode is present and is often characterized using the metric full-width at half-maximum (FWHM), which is the width of the peak at the point of intensity where it is half of the maximum intensity.

Chapter 3

VCSEL Dynamics

We have already established that VCSELs are a key component in OIs. The VCSEL is intensity modulated using current or voltage based drivers. In datacom, on-off keying (OOK) and 4-level pulse-amplitude-modulation (PAM4) are commonly used [55,56], but higher order modulation formats are also considered. This means that the VCSEL is switched between different intensity states, which are decoded into ones and zeros.

Since high data rates are used in combination with direct modulation, VCSELs used in these applications must have a high bandwidth and a proper frequency response, otherwise overshoot- and ringing effects as well as slow rise- and fall-times might increase the bit-error-ratio (BER) [57].

3.1 Intrinsic Response

The dynamics at play inside VCSELs, and semiconductor lasers in general, can be described by a set of rate equations, which take into account the processes behind and interactions between injected free carriers and photons in the cavity. Generally for a multi-mode laser, one would need to describe each mode separately with rate equations. However, for oxide-confined VCSELs with strong guiding and highly overlapping modes, it has been shown that a single set of rate equations is adequate for a first-order analysis of the intrinsic dynamics [58], as for a SM VCSEL. The rate equations can be written as follows [42]:

$$\frac{dN}{dt} = \frac{\eta_i I}{qV_a} - \left(AN + BN^2 + CN^3\right) - \upsilon_g GS, \tag{3.1}$$

$$\frac{dS}{dt} = \Gamma \upsilon_g G S - \frac{S}{\tau_p} + \Gamma \beta B N^2. \tag{3.2}$$

In these Equations, N and S are the excess carrier density in the active region and photon density in the cavity. η_i is the internal quantum efficiency, I the bias current, q the elementary charge, V_a the volume of the QWs, the A, B and C coefficients are the same as in Equation 2.4, υ_g is the group velocity, G the material gain, Γ the confinement factor, τ_p the photon lifetime and β the fraction of the spontaneous emission coupled into the lasing mode.

Another effect that is not written out in the Equations above is the gain compression, which represents the reduction of optical gain at high photon densities. This can be accounted for by expressing the gain as

$$G = \frac{G_0}{1 + \varepsilon S}, \tag{3.3}$$

where G_0 is the unsaturated gain and ε is the gain compression factor.

The intrinsic dynamic performance of a VCSEL can be characterized in several aspects using a small-signal analysis. In order to do this theoretically, Equations 3.1 and 3.2 are perturbed using a first order Taylor expansion. After solving for the small-signal frequency response, we end up with a second order system and the transfer function for the intrinsic response [42]

$$H_{int}(f) = \eta_d \frac{hc}{\lambda_0 q} \cdot \frac{f_r^2}{f_r^2 - f^2 + j\gamma \frac{f}{2\pi}}. \tag{3.4}$$

In this Equation, η_d is the differential quantum efficiency, h the Planck constant, c the speed of light, f_r the resonance frequency (defined below) and γ the damping factor (defined below). The resonance frequency f_r can be approximated as

$$f_r \approx \frac{1}{2\pi} \sqrt{\frac{\upsilon_g g_0 S}{\tau_p \left(1 + \varepsilon S\right)}}, \tag{3.5}$$

where g_0 is the nominal differential gain dG_0/dN. In order to push the resonance frequency higher, and thus potentially increase the bandwidth of the VCSEL, one can from the above expression deduce that a high differential gain, high photon density and a short photon lifetime are beneficial for this purpose. However, a higher photon density does not in an unlimited fashion equate to a higher modulation bandwidth, as

e.g. damping, thermal and parasitic effects also affect the response. Figure 3.1 shows how the response can qualitatively change with photon density, and also that a higher photon density does not provide a higher bandwidth beyond a certain point because of increased damping.

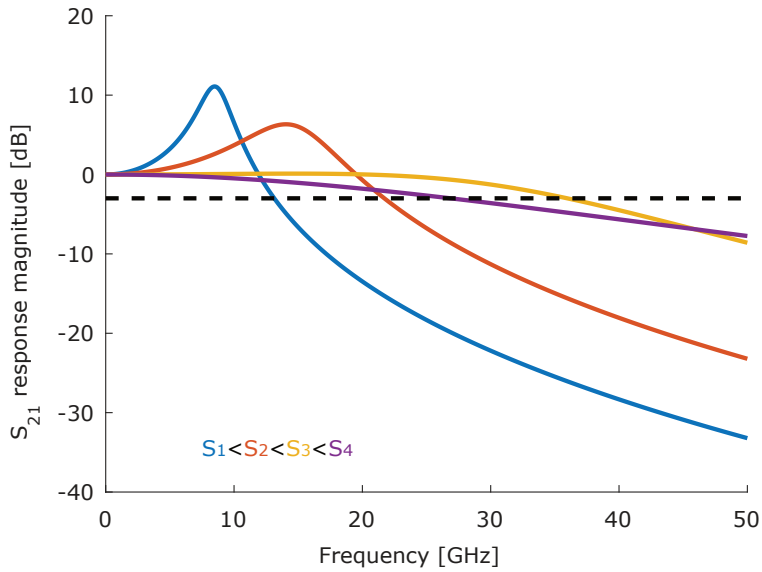

Figure 3.1: Intrinsic modulation response ($20\log_{10}(|H_{tot}(f)/H_{tot}(0)|)$) for a VCSEL with $\gamma_0 = 10\text{ns}^{-1}$, $f_p = 50$ GHz, $K = 0.2$ ns, with a S sweep (photon density). The dashed line indicates the -3 dB response, at which the intersection with the S_{21}-curves indicate the modulation bandwidth of the VCSEL.

The expression for the damping factor can be written as

$$\gamma = Kf_r^2 + \gamma_0, \tag{3.6}$$

where γ_0 is the damping offset and K the K-factor written as

$$K = 4\pi^2\left(\tau_p + \frac{\varepsilon\chi}{\upsilon_g g_0}\right), \tag{3.7}$$

where χ is referred to as the transport factor, defined as $\chi = 1 + (\tau_{cap}/\tau_{esc})$ where τ_{cap} is the time it takes for the free carriers to be

transported across the SCH and captured into the QWs, and τ_{esc} the escape time of the carriers from the QWs into the SCH [59], which is a main topic of Paper C.

The magnitude of the K-factor plays a substantial role in the damping of the VCSEL response, as seen in Figure 3.2, which shows the intrinsic modulation response of the VCSEL for several values of K, a higher K contributes to a more damped response. It is worth nothing that K is mainly controlled by τ_p.

Further, the increase of the resonance frequency with current, which is mentioned above, is quantified using the D-factor

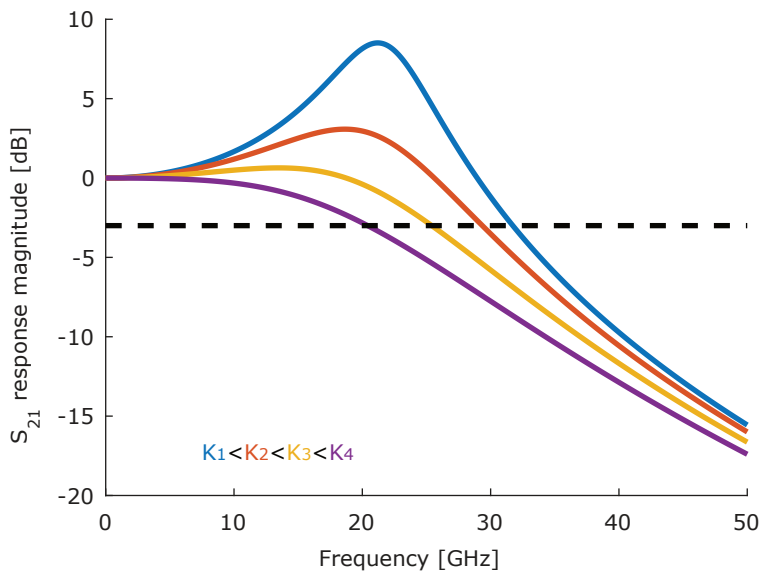

Figure 3.2: Intrinsic modulation response ($20\log_{10}(|H_{tot}(f)/H_{tot}(0)|)$) for a VCSEL with $\gamma_0 = 10\text{ns}^{-1}$, $f_p = 50$ GHz, with a K-factor sweep. The dashed line indicates the -3 dB response, at which the intersection with the S_{21}-curves indicate the modulation bandwidth of the VCSEL.

$$f_r = D \cdot \sqrt{I - I_{th}}, \quad \text{where} \quad D = \frac{1}{2\pi}\sqrt{\frac{\eta_i \Gamma \upsilon_g}{qV_a} \cdot \frac{g_0}{\chi}}, \tag{3.8}$$

where I is the injected current and I_{th} is the threshold current. From

this Equation we see that increasing the rate at which the resonance frequency increases with current requires a high confinement factor, high differential gain and low transport factor (free carriers need to be captured much faster than they escape).

An interesting aspect of trying to maximize the bandwidth by pushing the resonance frequency higher is that this process is limited by damping. Since $f_r \propto \sqrt{S}$ and $\gamma \propto S$, the VCSEL will with an increasing photon density at some point become more damped than the resonance frequency can compensate for and the modulation bandwidth will drop with increasing photon density beyond that point. The maximum damping-limited bandwidth in absence of thermal effects and parasitics can be approximated by (under the assumption that γ_0 can be neglected) [60]

$$f_{3dB}^{max} \approx \frac{2\sqrt{2}\pi}{K}. \tag{3.9}$$

3.2 High-Speed VCSELs

3.2.1 Design

While VCSELs inherently have a relatively high modulation bandwidth, many tricks can be used to mitigate effects that negatively impact the high-speed performance. The high-speed VCSEL differs from the simple VCSEL presented in Figure 2.3 in several aspects. A schematic high-speed VCSEL cross-section can be seen in Figure 3.3. First, the most apparent difference is the benzocyclobutene (BCB). This is a high-κ dielectric used for the purpose of lowering the pad parasitics (mainly capacitance). Secondly, the n-contact layer is etched away below the pad, in order to further reduce pad capacitance.

Another visible improvement in Figure 3.3 is the reduction of mesa (mainly oxide) capacitance, by employing a more complex oxide layer structure beyond a single layer. In our high-speed designs, two 98%-AlGaAs layers are used in order to form the oxide aperture for electro-optical confinement, and four 96%-AlGaAs layers in order to form secondary oxide apertures to further reduce the mesa capacitance [61].

The active region design is another important aspect of the high-speed VCSEL design. In order to provide a high resonance frequency to push the modulation bandwidth even for lower current densities as high as possible without having an under-damped VCSEL, a high D-factor

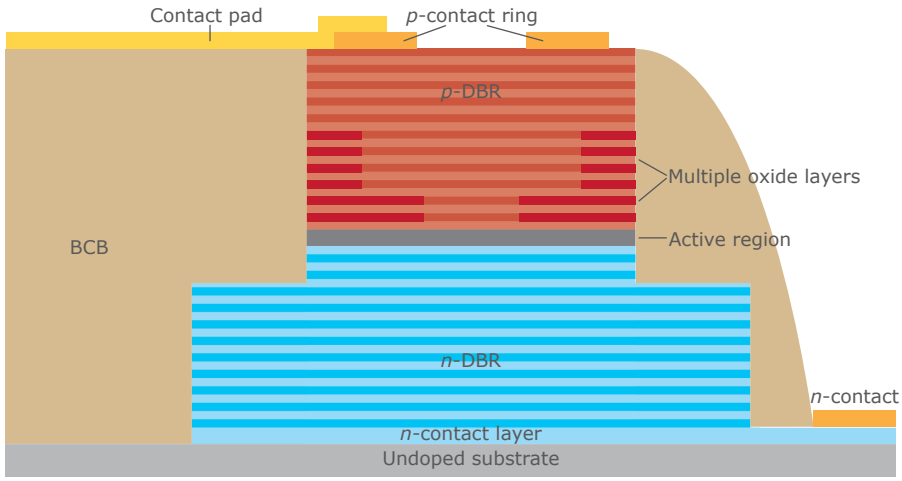

Figure 3.3: Cross-sectional schematic of a high-speed top emitting p-side up VCSEL, with 2+4 oxide layers/apertures.

is needed, which according to Equation 3.8 means a high differential gain, strong optical confinement and a low transport factor. In modern high-speed VCSELs this is commonly achieved using strained QWs [62]. In GaAs VCSELs, $In_xGa_{(1-x)}As$ QWs with an indium-content of a few percent with $Al_xGa_{(1-x)}As$ barriers can be used to achieve compressively strained QWs. This method, however, also affects the bandgap, and with increasing In-content the gain spectrum red-shifts. That is why more strained InGaAs/AlGaAs QWs are more easily achievable at longer wavelengths where the more strained QWs can provide higher differential gain at the target wavelength and therefore good performance in high-speed data transmission [63].

The main heat sources of VCSELs is resistive heating, internal optical absorption and carrier leakage effects [64]. Reduction of the thermal effects is important in high-speed VCSELs. Apart from the obvious solution of heatsinking the VCSEL itself, processing to achieve better heat conductivity through techniques such as electroplating mesa sidewalls with metal [65] or substrate removal and replacement by an electroplated metal substrate [66] have been employed. However, excessive metallization can introduce unwanted capacitance and lead to modulation bandwidth decrement. Further, the thermal conductivity of the AlGaAs-system is also relevant, as binary GaAs and AlAs have much higher thermal conductivities than AlGaAs with Al-concentrations

in-between [67]. Meaning that AlGaAs-DBRs with high and low Al-concentrations are beneficial for this purpose. However, GaAs is not transparent at a wavelength of 850 nm, AlAs can cause processing problems through unintentional oxidation, and low Al-content AlGaAs may cause band-to-band absorption at high temperatures, which means that trade-offs are necessary.

To lower the resistance of the DBRs, modulation doping and graded composition interfaces are used to ease carrier transport across the potential barriers. Proper modulation doping also minimizes free carrier absorption. Carrier leakage effects can be mitigated using proper transverse current confinement, and in the longitudinal direction by deeper QWs.

3.2.2 Parasitics

VCSELs, like other semiconductor lasers operating at high frequencies suffer from parasitic effects such as abundant capacitance, inductance and resistance. This can be modelled more or less accurately. Paper A presents a more comprehensive approach to modelling VCSEL parasitics. Therefore, to highlight the effects of parasitics on the VCSEL modulation response a more simple model is presented below.

Figure 3.4 shows a simple small-signal equivalent input impedance circuit that can be used to model a VCSEL's parasitic behaviour, similar to the work presented in [68]. This features a capacitor between the pad and lower parts of the VCSEL structure (depending on geometry and epitaxial structure), a capacitor to model the oxide and junction capacitances, simplified by using a single capacitor as these are mostly parallel. Finally, resistors to model the resistances of the DBRs (one lumped component approximating both DBRs) and the active region (junction). In such a model, the current flowing through the junction R_j-resistor would be the current generating excess carriers in the active region.

Because not all the current flows through R_j at high frequencies (partly shunted through C_m and C_p), the signal is RC-low-pass filtered, which can be modelled using a single-pole transfer function (if C_p can be neglected)

$$H_{par}(f) = \frac{1}{1 + j\dfrac{f}{f_p}}, \tag{3.10}$$

where f_p is the cut-off frequency representing the effects of parasitics.

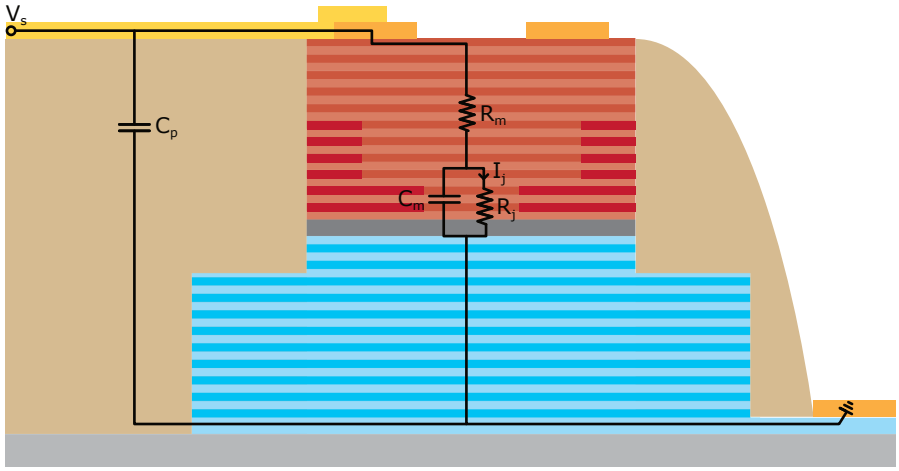

Figure 3.4: A simple small-signal input impedance circuit for a VCSEL.

More advanced input impedance models such as the one presented in Paper A might have different responses and not necessarily being a single-pole parasitic transfer function. Combining the simple parasitic transfer function with the intrinsic transfer function presented in Equation 3.4 yields a more accurate description of the total VCSEL transfer function:

$$H_{tot}(f) = H_{int}(f) \cdot H_{par}(f) = \eta_d \frac{hc}{\lambda_0 q} \cdot \frac{f_r^2}{f_r^2 - f^2 + j\gamma\frac{f}{2\pi}} \cdot \frac{1}{1 + j\frac{f}{f_p}}. \quad (3.11)$$

3.2.3 Large-Signal Performance

There are several considerations regarding VCSEL large-signal performance in high-speed data links. The end goal of achieving a low BER is dependent on a large number of factors, including the D-factor, K-factor, ambient temperature, VCSEL bias point, and in longer links the fiber. Other aspects to consider are the modulation format and driving signal shaping and pre-emphasis [69]. The receiver side is also important both in terms of frequency response, which can be mitigated through equalization, and in terms of forward-error-correction (FEC), two digital signal processing (DSP) techniques [69].

Both under- and overdamping of the VCSEL will diminish the performance by effects such as overshoot and ringing or slow rise/fall times

and low modulation bandwidth, see Figure 3.2 for examples of such frequency responses. This means that the frequency response of the VCSEL has to be properly adjusted for high-speed datacom applications, which can be done by adjusting the K-factor.

In practice, the optimal settings for bias point and driving signal at various temperatures have to be found experimentally, through systematic optimization with e.g. BER-experiments. However, efforts are being made, such as in Papers A–C in this thesis and other similar works, to fully model datacom VCSELs and thus ease the efforts of finding optimal VCSEL designs and settings for driving them.

3.2.4 Carrier Dynamics and Limitations

Paper C explores through simulations the impact of carrier transport and capture physics, but it is important, even in this introduction, to highlight the potential impact of carrier dynamics on the performance of high-speed VCSELs.

Starting during the 1990s, several studies have been conducted to investigate carrier transport, carrier capture and carrier leakage effects in QW lasers. Long time constants associated with carrier transport effects in the SCH, and carrier capture by the QWs can be associated with reduced bandwidth by a parasitic-like low frequency roll-off [70]. This causes longer effective capture times to be generally unfavourable for high-speed modulation applications, e.g. in datacom. The effective capture time is defined as

$$\tau_{cap,eff} = \tau_{cap,int} + \tau_{transport}, \tag{3.12}$$

where $\tau_{cap,int}$ is the intrinsic QW capture time and $\tau_{transport}$ the transport time in the SCH. Finally, it should be stated that in order to be able to account for transport effects, the rate equations presented in Equations 3.1 and 3.2 would need to be expanded with another rate equation that accounts for accumulation of carriers in the continuum of the SCH, as is done in Papers A–C.

3.2.5 Thermal Limitations

Thermal effects in high-speed VCSELs can not be neglected, as the VCSEL is a relatively high-resistance laser biased at currents far beyond threshold. This causes current-induced heating due to various effects

such as Joule heating, non-radiative recombination described in Equation 2.4, carrier thermalization and internal absorption. The D-factor decrement with increasing temperature (due to reduced g_0 and η_i), which can limit the resonance frequency increment rate before the bandwidth becomes thermally limited, can to some extent be mitigated. By changing the detuning and engineering the gain spectrum of the VCSEL, it can be made to have a lower threshold current at a higher temperature, thus increasing g_0 due to less electrical injection required to reach threshold. The higher g_0 at higher temperatures, however, comes at the cost of degraded low-temperature performance. This engineering is limited by next to unavoidable carrier leakage effects at high temperature which will lower η_i. Further, the D-factor and by extension the modulation bandwidth can be increased by operating the VCSEL on the short-wavelength side of the gain peak, as g_0 is higher there [71]. By evaluating the VCSEL transfer function with $\gamma = 0$, we find that the thermally limited bandwidth (in the absence of damping limitations and parasitics) is

$$f_{3dB}^{thermal} = \sqrt{1+\sqrt{2}} \cdot f_{r,max} \approx 1.55 f_{r,max}, \tag{3.13}$$

where $f_{r,max}$ is the maximum achievable resonance frequency.

The K-factor, as opposed to the D-factor is less temperature sensitive. As internal absorption increases with temperature due to increased free carrier absorption [72], the photon lifetime τ_p shortens [73], and looking at Equation 3.7 one can note that this can to some extent compensate for the lower differential gain associated with the increased temperature, which is also shown in [73].

3.3 Noise

There are several types of noise present in lasers, some more and less important to consider, entirely depending on laser type and application. Phase noise is a type of noise stemming from the random phase of spontaneous emission photons coupled into the lasing mode. This noise type is the main origin of the linewidth of single mode lasers. Hence, phase noise is often the limiting type of noise in applications requiring coherence or spectral purity [74]. However, for datacom applications, phase noise can usually be neglected since MM VCSELs are commonly used.

For datacom applications the limiting type of noise is intensity noise, which is quantified by comparing the noise power to the laser CW power,

from which the term relative intensity noise (RIN) stems, an important aspect of Paper B. While the main source of this noise can be approximated using spontaneous emission models [75], it can also, as in Paper B, be treated as a noise created by temporal uncertainty of the processes which take place inside the VCSEL, such as transport, trapping, annihilation or escape of carriers and absorption, generation and loss of photons [76]. Intensity noise essentially degrades the signal-to-noise-ratio (SNR) in direct-detection systems by adding unwanted intensity fluctuations that ultimately reduce the BER by introducing errors when decoding the signal.

When measuring intensity noise, other sources of noise than just the laser RIN have to be taken into account. One being shot noise, which is caused by the temporal randomness of photons arriving at the detector [77]. The system also has thermal noise, caused by the active components (e.g. amplifier) and non-zero Kelvin temperature resistors. Both of these have to be accounted for when measuring the laser RIN.

3.4 Measurement Setups

All of the small-signal, large-signal and RIN measurements setups include a few elements. In all of them, the VCSEL is placed on a Peltier element, which is temperature controlled. The beam is picked up using a fiber, which technically can be a cleaved fiber or lensed fiber, however we use an AR-coated lens-package to couple the beam into the fiber (typically OM4) with an APC-type connector. A variable optical attenuator (VOA) is optional unless BER-measurements are performed or the PD is power limited. The PD is also bias-monitored, which allows for the generated DC (direct current) photocurrent to be measured, which is of importance when measuring laser RIN. Apart from these common elements, the three measurement setups are explained in the upcoming Sections.

3.4.1 Small-Signal Measurement Setup

See Figure 3.5 for a block diagram of the measurement setup. The small-signal measurement measures the frequency response of the VCSEL. The signal is supplied to the VCSEL from a port (1) on the vector network analyzer (VNA), through a bias-T, where it is combined with a DC bias current. The bias-T is built-in in some VNAs. The PD signal is fed back to a different port (2) on the VNA. The VNA performs the

characterization by supplying a small magnitude sine signal, in order to operate the VCSEL under small-signal conditions, which is frequency-swept and the VNA measure how much of it arrives at the second port for an S_{21}-measurement. The probe and PD responses have to be taken into account when calculating the final S_{21} response. An S_{21} measurement captures the full response of the VCSEL, including parasitic effects. For an S_{11} measurement, only one port is required, as this is a measure of the voltage that is reflected back. The calibration used for the reflection measurement is of the short-open-load type, where a calibration chip compatible with the probe is probed at different points in order to show the VNA how the response looks when probing an electrically shorted structure, open structure and a (often) 50 Ω load.

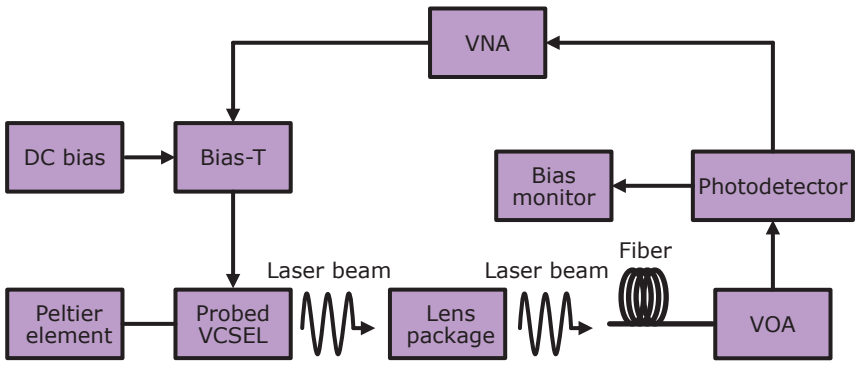

Figure 3.5: Block diagram of a system used to measure the VCSEL small-signal response.

3.4.2 Large-Signal Measurement Setup

See Figure 3.6 for a block diagram of the measurement setup. The VCSEL is driven with a signal generated by a bit pattern generator (BPG), which passes through a bias-T to be combined with a bias current. The PD is connected to an amplifier in order to amplify the signal before electrical detection. In the block diagram, two paths are indicated, path A for eye diagram capture and path B for BER measurements. For the eye diagram measurements, the signal is fed to an oscilloscope, which records the signal and displays it in the form of eyes by superimposing data steams (see Papers A–C for examples). For the BER measurements,

the amplified signal is recorded by an error analyzer (EA) and compared to the output of the BPG in order to evaluate the BER. For both measurement types, a clock is required to set the rate and synchronize the oscilloscope, BPG and EA. If needed, when the signal exits the BPG, it can also be amplified. An arbitrary wave generator (AWG) can be used to generate the signal instead of a BPG. The PD and amplifier can be substituted by a photoreceiver.

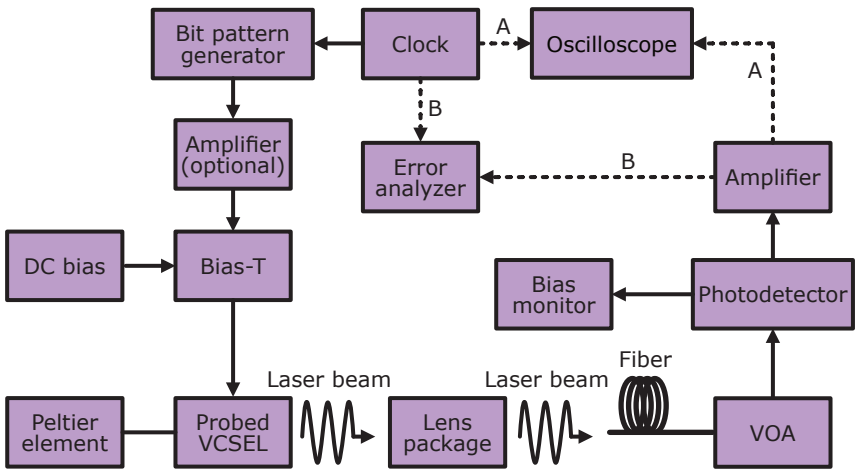

Figure 3.6: Block diagram of a system used to measure the VCSEL large-signal characteristics, path A for eye diagram measurements and path B for BER measurements.

3.4.3 Relative Intensity Noise Measurement Setup

See Figure 3.7 for a block diagram of the measurement setup. The VCSEL is fed a DC current, and the signal detected at the PD is fed to an amplifier, from which the output is characterized by an electrical spectrum analyzer (ESA). The noise properties of VCSELs are sensitive to optical feedback and great care has to be applied in order to avoid feedback effects. As mentioned in Section 3.3, both shot noise and thermal noise have to be subtracted when calculating the RIN of the VCSEL, as the ESA will inevitably record all three of those.

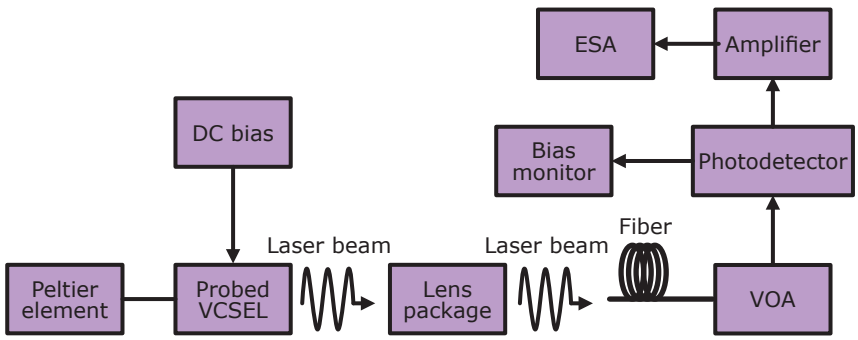

Figure 3.7: Block diagram of a system used to measure the VCSEL RIN.

Chapter 4

VCSEL Modelling

4.1 Overview

More advanced VCSEL modelling for large-signal simulations started back in the 90s, as an extension of the previous QW-laser modelling work, with the most prominent models published by P.V. Mena [78, 79].

While analytical methods may be sufficient for more simple analysis of VCSELs, and lasers in general, numerical methods are required to properly describe the large-signal modulation response, as many interlinked effects have to be taken into account and the equations need to be propagated in time.

The modelling itself is motivated by optimization of the electronic IC driving the VCSEL, and also full-system simulations and optimization, as all components have to work together. During recent years, when bandwidths of both the VCSELs and PDs have stagnated around 30 GHz, it has become increasingly important to co-optimize the VCSEL with the rest of the link.

4.2 Previous Work

This Section provides a few examples of earlier VCSEL-modelling work, mainly focused on the large-signal domain. This can be found in references [78–92]. All of these are rate equation based circuit-level implementations, with the exception of [84,85], which are based on a numerical behavioural model. Below follows comments on some of the works and their applications.

As mentioned earlier, in [78], P.V. Mena presented one of the first

comprehensive VCSEL models with improvements in [79]. This is a circuit-level model implemented in a SPICE-like simulator, based on rate equations and takes into account both thermal and spatial effects, which is an improvement from the earlier QW-laser models.

In [80], a model similar to Mena's is presented, however with small modifications to aid convergence for the circuit-level implementation. Further, a Volterra series-based model was presented in [80], and compared to a neural network implementation, both of which have the potential to be more suited for system-level simulations than circuit-level models, perhaps with the exception of driver optimization.

The model presented in [81] is quite similar to Paper A, also accounting for carrier transport effects. However, it uses a slightly different input impedance circuit, a passive one instead of a voltage source representing the voltage drop over the active region as was done in Paper A. It also uses a more simple noise implementation than Paper B. An extended version of [81] was used in [82], for optimizing launch conditions into an optical fiber. Further, in [83] it was also used for increasing the bandwidth-distance product in a datacom link.

In [90], an investigation into the effects of parasitics on VCSELs under multi-level modulation is presented. In [91], the model is used to present an extensive framework for optimizing driver circuitry.

4.3 VCSEL Model Building Blocks

As seen in the previous Section, there exist several approaches to model VCSELs. However, apart from implementations such as neural networks or Volterra series, VCSEL models are typically based on either numerical or circuit-level rate equation implementations. These often contain certain building blocks, which account for different behavioural aspects of the VCSEL.

Undoubtedly, the most fundamental building blocks of the VCSEL are accounting for carriers and photons, and their interaction. The model needs to keep accurate track of carriers in the QWs, and photons in the resonator, as this is important for calculating the rates of stimulated and spontaneous emission and the output power.

Further, adding thermally dependent parameters and keeping track of current-induced self heating is important, as VCSELs experience a large amount of self-heating due to relatively high current densities and resistance.

Parasitics in the form of resistances are important to provide the current-voltage relation, however, capacitive and inductive effects are important for high-speed application models in order to filter the drive signal and provide the corresponding input impedance.

For high-speed applications, it is also beneficial to introduce a second carrier reservoir for the carriers in the SCH continuum states, as this allows for, as explored in Paper C and mentioned in Section 3.2.4, introduction of a realistic parasitic-like frequency roll-off which stems from the delay related to carrier transport and QW capture effects.

Chapter 5

VCSELs on Silicon Nitride Photonic Integrated Circuits

The sub-field of photonics dedicated to light generation, transmission, manipulation and detection on silicon is referred to as silicon photonics (SiP or SiPh). This is achieved using photonic integrated circuits (PICs) on e.g. silicon-on-insulator- (SOI) or silicon nitride-based (SiN, SiNx or sometimes Si_3N_4) waveguide (WG) systems/platforms, which can be realized on CMOS-compatible wafers. CMOS stands for complementary metal-oxide-semiconductor, which is the main technique for fabrication of integrated electronic circuits, and therefore also an extremely mature technology. This is highly beneficial as SiP PICs can then be produced at a low cost at high volumes in CMOS fabs.

However, silicon has an indirect bandgap, and therefore efficient light generation is not possible. Although some progress with direct bandgap hexagonal SiGe-structures was recently reported [93], constituting a step towards V-material-system (e.g. Si, Ge) lasers, such light sources will likely not be available for large scale integration in the near future. Therefore, efforts have been focused on integration of other material-system light sources on PICs, mostly III-V materials (e.g. AlGaAs and InGaAsP). In this thesis and Paper D, the focus is on integration of GaAs-based VCSELs on SiNx PICs, as these are low-loss in the near-IR (near-infrared) [94] and therefore suitable for e.g. certain bio-photonic sensing applications.

Apart from low-loss waveguides, basic photonic components such as couplers/splitters, grating couplers (GCs), modulators, detectors, multiplexers and demultiplexers have been demonstrated [95,96], constituting

a rich photonic device library. Applications include i.e. coherent optical communication transceivers [97], sensing [98], biosensing [99], spectroscopy [100] and datacom links [101].

5.1 Integration Techniques

Growing III-V materials directly on silicon is challenging due to the mismatch of several material parameters, such as the lattice constant and thermal expansion coefficient. However, this can be achieved through epitaxial growth in trenches [102], utilizing aspect ratio dependent defect trapping, and while successful, this method is far from commercially viable. Furthermore, quantum dot lasers grown on silicon have been shown to be a good option [103].

Heterogeneous integration of III-V materials and lasers is a more mature technology. This primarily includes pick-and-place and bonding techniques. There are several pick-and-place techniques available, these are, but not limited to: butt-coupling, flip-chip and micro-optical benches. Butt-coupling [104] usually involves a die-level process, requiring precise alignment of the die-component to the PIC, for high coupling efficiency. Flip-chip [99,105] integration is based on flipping the die over, upside down, and soldering it to the target. This is done by placing the die on solder balls, either in a flat fashion or at an angle and reflowing the solder. The light from flip-chipped devices can be redirected either directly or at an angle onto a GC. However, this method suffers from relatively low throughput and scalability. Micro-optical-benches [106] features integration of an ensemble of micro-optical components in a single miniature module. This module is then placed on the PIC, and wire-bonded. Due to its integrated optical components, it can be, for example, integrated on top a GC.

There are also bonding-type integration methods, which can be divided into direct bonding and adhesive bonding. Bonding can be used for both die-to-wafer bonding and wafer-to-wafer bonding [107–109]. Direct bonding [110] works by means of Van Der Waals-forces, and requires thorough cleaning and surface treatment procedures of both the Si- and III-V-surfaces. Even small defects can create bonding problems when using this method, especially for direct wafer-to-wafer bonding, as the area is larger than for die-to-wafer bonding. Adhesive bonding [109, 111] is typically done with divinylsiloxane benzocyclobutene (DVS-BCB) as the bonding agent. This also mitigates issues related to defects, non-perfect

cleaning and non-planar surfaces such as roughness or structures.

For VCSELs, the so far most common integration methods are flip-chip [105,112] and bonding [109,113]. However, in the upcoming Section and in Paper D, we present integration through a different, and more scalable method.

5.2 Micro-Transfer-Printing

Compared to most other integration techniques, micro-transfer-printing (MTP) is a target material-independent, cost-efficient, easily scalable and mass fabrication friendly technique to transfer and integrate microscale devices [114, 115]. MTP offers high alignment accuracy, ± 1.5 μm, 3 σ [116]. This technique is demonstrated for VCSEL integration in Paper D, where the demonstration of fully functional GaAs-based VCSELs transfer-printed on SiNx PICs is the first of its kind.

5.2.1 Principles

First, the devices on the source substrate need to be secured in place using resist-based tethers, which allows for chemical access to a release layer. This is followed by releasing the devices via selective wet etching of the release layer underneath, which suspends the devices in air. The devices can then be transfer-printed. MTP is performed using a print head, with a stamp attached to it. The stamp is made of polydimethylsiloxane (PDMS) and the layout is tailor-made to match the layout of the devices that are being picked up. The PDMS stamp is aligned to, makes contact and adheres to the devices, which are then picked up by lifting the stamp quickly, which breaks the tethers. The devices are then aligned and placed on the target substrate, and can optionally be placed on e.g. DVS-BCB to aid bonding [111]. The stamp is then lifted slowly, which leaves the devices on the target. This is possible due to the special kinetic/elastometric properties of these stamps, which make the devices stick when the stamp is lifted quickly, and release when it is lifted more slowly [117].

5.2.2 VCSEL Design

The VCSELs to be transfer-printed have to be designed keeping the transfer-printing process and the application in mind. For the work in Paper D, full bottom-emitting VCSELs with two epitaxial DBRs were

printed. The design requires, most of all, a release layer. Such a layer has to be lattice-matched to the VCSEL's epitaxial layers, since these layers are grown on top of the release layer, and it has to be a material that can be etched selectively against the material system of the VCSEL or at least the layer directly above the release layer if the VCSEL is otherwise protected during fabrication. In Paper D, this was achieved using an InGaP release layer ($In_{0.49}Ga_{0.51}P$), which can be selectively etched against the $Al_{0.12}Ga_{0.88}As$ phase layer (also referred to as buffer layer in Paper D) with concentrated hydrochloric acid. A schematic of the design can be found in Chapter 6, Figure 6.1.

Chapter 6

VCSEL Fabrication for Micro-Transfer-Printing

The work in Paper D was performed with a metal-organic chemical vapor deposition (MOCVD) epitaxial VCSEL structure on an n-doped GaAs substrate. As we process small wafer-pieces, the text in this Chapter refers to partial-wafer processing instead of full-wafer processing, as is done in industry. Fundamentally, partial-wafer processing is not very different from full-wafer processing. Further reading on fabrication techniques and details can be found in [118].

6.1 Photolithography

One of the core processing steps of any micro-fabrication processes is lithography. As there are many forms of lithography and only ultraviolet (UV) photolithography is used in this thesis, the focus of this introduction is on this particular technique. The general idea behind any lithography is the transfer of a pattern onto a resist. For photolithography this is done using UV light and the transfer of the pattern is done onto a photoresist, which is a resist that is sensitive to UV light. The photoresist is generally used for protecting the wafer during physical or chemical etching (Section 6.2), as well as for lift-off of various thin films (Section 6.3). Lift-off refers to the dissolvement of the resist (in a solvent), which lifts the deposited material on top of it but leaves the rest behind.

In order to pattern the photoresist it first has to be spin-coated onto the wafer. The wafer is first coated with a thick layer of photoresist. The

wafer is then spun at a few 1000s rotations per minute which creates an even and thickness-controlled layer of resist. The thickness depends on the resist viscosity and spinning speed, where each resist has its own specifications. After this, the wafer is baked for a few minutes at a temperature of around 100-130°C in order to make the resist less sticky and improve the adhesion to the wafer by evaporating some of the solvent.

After this, the photoresist on the wafer is exposed to UV light (in our case 365 nm [i-line], 405nm [h-line], and 436 nm [g-line]), however, exposing all of it would defeat the purpose and therefore the resist needs to be patterned. Several patterning techniques are available, but two are fairly common. The first is contact photolithography, where the wafer with the photoresist is aligned and pressed against a quartz glass mask with metal patterns, typically chrome. The patterns are used to block light from passing while the clear areas of the quartz lets light through. When the wafer is aligned and in contact with the mask the wafer is exposed through the mask, using UV light. The second common technique is using a laser writer to write the pattern into the resist.

After this, the wafer is subjected to a photodeveloper liquid. For positive resists, the photodeveloper will dissolve all the UV-exposed photoresist, and for negative resists, it will dissolve the unexposed areas. A third option is usage of an image reversal resist, which after exposure also requires baking and full-wafer UV-exposure steps. The developer will then dissolve all the initially non-exposed areas of the resist. The image reversal resist is often used as a ”negative resist”, but due to the different chemical function will create a resist pattern with undercut, that allows for a cleaner lift-off procedure.

The resolution of photolithography depends on several system parameters, but is often limited by the wavelength of the light, and realistically UV photolithography can be used to pattern resists with a minimal feature size of 1 μm [118]. There is also a margin of error for the alignment of the mask to the wafer, which is also on the order of about 1 μm.

6.2 Etching

There are both wet and dry etching techniques that can be used to etch the AlGaAs-system and SiNx, used for the VCSEL fabrication. Wet etching is done using liquids to chemically dissolve materials. Although it is to some extent selective, it is hard to perform anisotropic wet etching, which is desired for e.g. the mesa etch, and it can also be hard to control

the etch rate and achieve consistency from run to run. Dry etching on the other hand makes use of chemical gases, often in plasmas which can also provide a physical etch, and provides better anisotropy than wet etching, however often at the cost of selectivity.

In Paper D, apart from wet etching to remove unwanted surface oxides, only dry etching was used. The technique used is the inductively coupled plasma (ICP) reactive-ion etch (RIE), in which a plasma of reactive gases is created, and the ions accelerated toward the wafer, where they chemically react with the target material and remove it from the exposed surfaces. For AlGaAs etching, a combination of $SiCl_4$ and inert Ar is used to create a chemical and physical etch of the material. For etching of SiNx, NF_3 gas is used to mostly chemically etch the SiNx. This system also has an in-situ laser interferometer monitoring system, which allows for a controlled etch depth.

However, ion beam etching (IBE), a purely physical etch in which Ar ions are accelerated and physically etch the target, was also used for testing and investigation purposes in this work.

6.3 Thin Film Deposition

During the VCSEL fabrication process, several metal and dielectric thin films are deposited, often with a maximum thickness of 500 nm and most commonly lower. The most used dielectric for (our) GaAs VCSELs is SiNx, but SiO_2 could also potentially be used. During the fabrication process, metals such as gold, titanium, platinum, nickel and germanium are used. There are several different ways of deposition, both physical and more chemical.

One physical deposition method is sputtering, which involves a metal or dielectric target which is physically bombarded with an Ar-plasma to rip the atoms from the target and physically deposit them on the wafer placed below. For a silicon-target, N_2 as a reactant is used to form Si_3N_4. A DC bias is applied to the target if it is conductive, or, for non-conductive targets, RF-sputtering (radio frequency) is used. This method provides excellent step coverage and good adhesion.

Another physical deposition method is evaporation. The material, commonly a metal or semiconductor, is placed in a crucible which is heated using either resistive Joule heating or electron beam heating where accelerated electrons hit the material. This heats up the material until it starts to evaporate, above which the wafer is placed upside-down,

and covered with the evaporated material. This method provides worse step coverage than sputtering, but is therefore more lift-off compatible. Evaporation provides good uniformity, and better opportunities for in-situ film thickness control.

One chemical method is called chemical vapor deposition, where gases are pushed into a reactor to then deposit on the wafer. In our case it is often plasma enhanced, yielding the plasma-enhanced chemical vapor deposition (PECVD) process, which is used for SiNx deposition. In this method, gases are injected into the reaction chamber, in which a plasma is generated, in our case using ICP. The gases injected into the chamber are made more reactive by the plasma, and in the case of SiNx-deposition a silane gas (SiH_4) is used to create a reaction with N_2, which is aided by the Ar ions in the ICP. The etch system also has an in-situ laser interferometer monitoring system, which allows for thickness control.

6.4 Selective Wet Oxidation

The oxide layer in the VCSEL is created using an oven with water vapor inside, reaching a temperature of 420°C. This is achieved by feeding N_2 through a water bubbler, which pushes water vapor into the oven. This process is sensitive to temperature changes, and therefore any temperature gradients, which can create a gradient in the oxidation rate across the wafer [119]. In order to mitigate this effect, the wafer is rotated 180°C after half of the oxidation time. The typical oxidation rate for $Al_{0.98}Ga_{0.02}As$ in our system varies from 0.15 μm/min to 0.40 μm/min due to process and epitaxial variations (varying Al-content), but is typically in the 0.25-0.30 μm/min range. The oven has a glass window which allows for in-situ monitoring of the oxidation process using an infrared CCD camera (charged-coupled device) and diode illumination system, which is based on the difference in reflectivity between oxidized and non-oxidized AlGaAs.

6.5 Process flow

In this Section, the process flow used for fabrication of VCSELs for the micro-transfer-printing integration performed in Paper D is described in more detail. See Figure 6.1 for cross-sectional schematics. First, the epitaxial material is cleaved into wafer pieces and cleaned using solvents [Subfigure (a)]. Then, *p*-type contacts made of layered Ti/Pt/Au in the

form of annuli (rings) are deposited through evaporation and lift-off on the topmost DBR layer. The contacts can also be circular to act as reflectors, as was done in Paper D, however the drawback is that the output power cannot be monitored through the top [Subfigure (b)]. After this, a circular hard mask is created from etching sputtered SiNx using a NF_3-based ICP RIE dry etch for the purpose of top mesa etching. After this, another ICP-RIE dry etch using $SiCl_4$ and Ar to form the top mesa is performed and a SiNx protective layer is subsequently deposited using PECVD [Subfigure (c)]. The protective layer of SiNx is then opened at the top mesa sidewall using an ICP RIE NF_3 etch and the VCSEL is subsequently subjected to selective wet oxidation [Subfigure (d)]. Further, the SiNx is removed by an ICP RIE NF_3 etch and Ni/Ge/Au *n*-type contacts are deposited using evaporation and annealed at a temperature of 390°C [Subfigure (e)]. Another ICP RIE $SiCl_4$/Ar etch is then performed to create a bottom mesa, etching down to roughly half of the phase layer in order to avoid affecting the release layer before release (which is done using selective wet etching), after which a protective and passivating SiNx layer is deposited using sputtering [Subfigure (f)]. Finally, the SiNx layer is opened up at the top surface and on the *p*- and *n*-contacts using ICP RIE NF_3, which are metallized with sputtered Ti/Au contact pads for easier access in further processing (or pre-transfer-print testing) [Subfigure (g)].

Details on the transfer-printing and post-processing beyond the on source-wafer VCSEL fabrication, can be found in Paper D and [120]. In summary, the VCSELs are anchored from all four x-y-directions using resist-based tethers. This is followed by etching through the phase layer, down to the release layer which is fully removed using selective wet etching, and the VCSELs become suspended in the air using the tethers. After this, the VCSELs (one or several, depending on stamp layout, which is tailor made) are picked up using a PDMS stamp. They are then placed on the target PIC, on top of GCs, with a thin BCB layer for adhesive bonding in-between. The VCSELs are finally planarized with BCB and metallized with contact pads for probing or wire bonding.

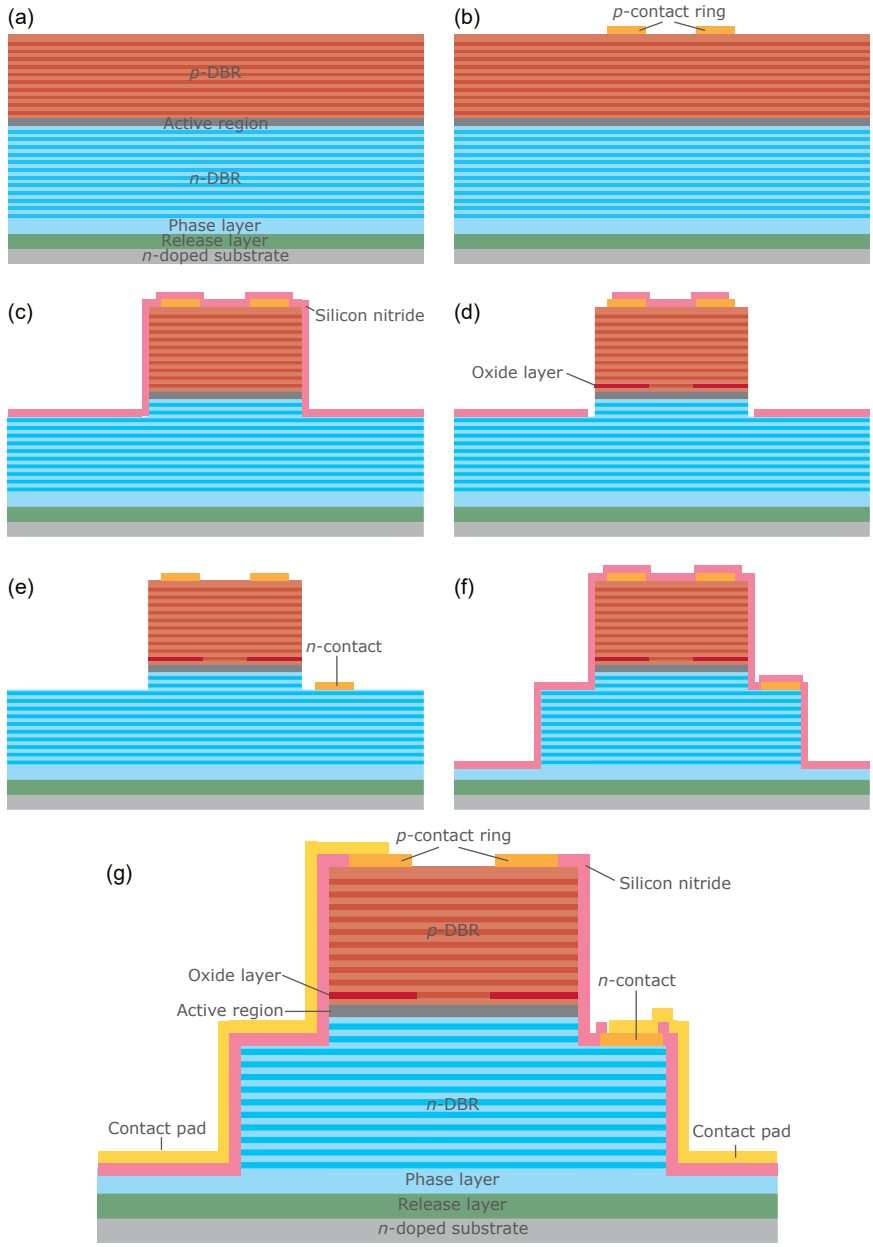

Figure 6.1: The processing steps of a *p*-side up bottom emitting VCSEL designed for micro-transfer-printing, (a) showing the starting epitaxial structure and (g) showing a functioning but not yet transfer-printed VCSEL.

Chapter 7

Outlook and Future Work

7.1 Datacom VCSELs

There are several interesting potential future developments of the research behind Papers A–C, on VCSEL modelling, related to datacom applications. As previously described in Chapter 4, many VCSEL models have been developed throughout the years. However, one interesting aspect is that there is a lack of published large-signal high-speed VCSEL models for very broad temperature ranges, suitable for both cold (-40°C) and very hot environments (125°C). This temperature range is not a coincidence, but rather a requirement for applications in the automotive industry (-40°C to >100°C) [121] and the datacom industry (room temperature to >100°C) [122] when optical transceivers are co-packaged with ASICs (application-specific integrated circuits) used for computing and switching, or even applications such as radars, that have to be very temperature-resilient. Currently, in this area, our GaAs VCSEL research group is working on developing VCSELs for harsh environments such as the above-mentioned ones. Extending the working temperature range of the VCSEL model presented in Papers A–C would be a large improvement, as it will aid the development of full optical transceivers for an extended temperature range.

Further, the model is, as standing, a single-mode approximation. It can, however, for the future be expanded to use a multi-mode description of the VCSEL, and be useful for longer reach optical interconnects, as this would allow for tracking of different VCSEL modes and better estimation of the effect a given fiber will have on the signal.

7.2 VCSELs for SiNx PICs

While we have in Paper D provided a first time demonstration of MTP GaAs VCSELs on SiNx PICs, these results can certainly be improved. The results presented are essentially the second iteration of working devices, although they already work above the minimum specifications for the target sensing application. Due to the Covid 19-pandemic and various delays, the final iteration had to be somewhat straightforward and less time was spent on optimization of details.

The performance before printing was good in terms of thermal roll-over current, however after printing, the thermal properties degraded substantially. Further improvement must be done to manage thermal effects on the PIC.

Finally, the concept behind Paper D can certainly be used in more applications than just sensing, where VCSELs are micro-transfer-printed onto PICs. For example, datacom applications seem interesting, as MTP would be beneficial considering the large device volumes of the datacom industry. For example, dense MTP of a large number of high-speed VCSELs at multiple wavelengths on the PIC, where wavelengths are multiplexed on a number of spatial channels, would enable compact and energy efficient transmitters with very high aggregate capacity.

However, as silicon photonics is still a rapidly developing field, it is hard to say exactly what the future might bring.

Chapter 8

Summary of Papers

PAPER A

"Large-Signal Equivalent Circuit for Datacom VCSELs", *IEEE/OSA Journal of Lightwave Technology*, vol. 39, no. 10, pp. 3225-3236, May 2021, doi: 10.1109/JLT.2021.3064465.

This paper presents a physics-based equivalent circuit model for datacom VCSELs, capable of accurately predicting the large-signal modulation response under different conditions. The work is motivated by bandwidth stagnation of optoelectronic components, which requires co-design and co-optimization with driver and receiver electronics to enable higher data rates. The model accounts for the impedance of the VCSEL and tracks the carriers in the separate-confinement heterostructure and the quantum wells, thereby accounting for carrier transport and capture effects. The model also accounts for current-induced self-heating effects and gain compression. Simulations are compared with measurements for verification purposes. Excellent agreement over a broad range of parameters, such as bias current, temperature and modulation format, is achieved in terms of both static and dynamic VCSEL behavior.

My contribution: I co-developed the model with Johan Gustavsson (JG) and I implemented the model in the software. I performed all circuit simulations and measurements and extracted circuit parameter together with JG. Me and JG co-authored the paper, with me as the lead author.

PAPER B

"Large-Signal Equivalent Circuit for Datacom VCSELs - Including Intensity Noise", Accepted for publication in *IEEE/OSA Journal of Lightwave Technology*, doi: 10.1109/JLT.2022.3200905.

This work presents an extension of the model presented in Paper A, with intensity noise added. Noise is added separately to each of the physical processes in the model, assuming Poisson noise processes and white noise in the frequency domain, thus Gaussian noise in the time domain. However, the white noise generated by each process propagates through the circuit, thus being shaped in the frequency domain. The paper also features more accurate large-signal full link simulations, including more complete models for the photoreceiver, with relevant noise properties. Relative intensity noise measurements and simulations are compared to verify the noise levels in the frequency domain. All simulations show good agreement with measurements.

My contribution: I co-developed the model with JG and I implemented the noise extension of the model. I performed all measurements and simulations. Me and JG co-authored the paper, with me as the lead author.

PAPER C

"Impact of Carrier Transport and Capture on VCSEL Dynamics", Submitted to *IEEE Journal of Quantum Electronics*.

This study investigates the impact of carrier transport and capture on VCSEL dynamics using the model in Paper A, an impact that is next to impossible to study experimentally. The study finds that the effective capture time can have large impact on the VCSEL small- and large-signal modulation response. With increasing effective capture time, a clear decrease of bandwidth is observed, which results in longer rise- and fall times, closing the optical eyes in the vertical direction. However, a too short effective capture time leads to timing jitter and intersymbol interference because of the under-damped response. It is concluded that for a given effective capture time, which should be as short as possible to enable the highest modulation speed, the photon lifetime should be set to balance the effects for a critically damped, high-bandwidth response.

My contribution: I performed all simulations and most of the analysis, and I am the main author of the paper.

PAPER D

"Enabling VCSEL-on-silicon nitride photonic integrated circuits with micro-transfer-printing", *Optica*, vol. 8, no. 12, pp. 1573-1580, Dec 2021, doi:10.1364/OPTICA.441636.

This work presents a technique for micro-transfer-printing of GaAs-based 850 nm VCSELs on silicon nitride PICs, which enables cost-efficient integration of an energy efficient light source, compatible with high-volume manufacturing. Fully functional bottom-emitting VCSELs are processed on the GaAs source wafer, followed by under-etching and release after anchoring to the source wafer by tethers. A stamp is used to pick up the VCSEL coupon from the source wafer and transfer to the SiN PIC target wafer where it is attached over a grating coupler using adhesive bonding. The PIC is developed for a bio-sensing application. Therefore, the grating coupler is designed for bi-directional coupling to enable optical powering of several sensors on the PIC. A waveguide-coupled optical power exceeding 100 µW with sub-mA VCSEL threshold current is demonstrated. Since the application requires spectral purity and wavelength tunability, the VCSEL is single-mode and the wavelength is tuned by the VCSEL current. A suppression of higher order modes by >45 dB and a tuning range of 5 nm were achieved. In addition, for efficient coupling to the waveguide, the polarization of the VCSEL has to be aligned to the grating lines. This is achieved by polarization selective optical feedback from the grating coupler, which required VCSEL-grating coupler co-design.

My contribution: Me and Jeroen Goyvaerts (JGo) collaborated closely and contributed equally. We co-authored the paper. I developed the VCSEL fabrication process, fabricated pre-processed VCSELs on the source wafer and delivered to Ghent University for subsequent transfer printing on SiN PICs by JGo who also developed the PIC. The PICs were fabricated at imec. JG assisted with VCSEL design. I performed many of the measurements, including most notably spectral and polarization measurements and measurements to assess performance over temperature.

References

[1] Cisco. (2019) Cisco Visual Networking Index: Forecast and Trends, 2017–2022. (Accessed: 2022-07-08). [Online]. Available: https://twiki.cern.ch/twiki/pub/HEPIX/TechwatchNetwork/HtwNetworkDocuments/white-paper-c11-741490.pdf

[2] ITU. (2015) IMT traffic estimates for the years 2020 to 2030. (Accessed: 2022-07-08). [Online]. Available: https://www.itu.int/dms_pub/itu-r/opb/rep/R-REP-M.2370-2015-PDF-E.pdf

[3] The World Bank. (2020) Individuals using the Internet (% of population). (Accessed: 2022-07-06). [Online]. Available: https://databank.worldbank.org/reports.aspx?dsid=2&series=IT.NET.USER.ZS

[4] Cisco. (2020) Cisco Annual Internet Report (2018–2023). (Accessed: 2022-07-08). [Online]. Available: https://www.cisco.com/c/en/us/solutions/collateral/executive-perspectives/annual-internet-report/white-paper-c11-741490.pdf

[5] Sebastian Moss, Data Centre Dynamics. (2022) In search of the world's largest data center. (Accessed: 2022-09-18). [Online]. Available: https://www.datacenterdynamics.com/en/analysis/in-search-of-the-worlds-largest-data-center/

[6] IAEA. (2021) What are Small Modular Reactors (SMRs)? (Accessed: 2022-09-18). [Online]. Available: https://www.iaea.org/newscenter/news/what-are-small-modular-reactors-smrs

[7] Cisco. (2018) Cisco Global Cloud Index: Forecast and Methodology, 2016–2021. (Accessed: 2022-09-14). [Online]. Available: https://virtualization.network/Resources/Whitepapers/

0b75cf2e-0c53-4891-918e-b542a5d364c5_white-paper-c11-738085.pdf

[8] W. H. Hofmann, P. Moser, and D. Bimberg, "Energy-Efficient VCSELs for Interconnects," *IEEE Photonics Journal*, vol. 4, no. 2, pp. 652–656, 2012.

[9] A. Larsson, "Advances in VCSELs for Communication and Sensing," *IEEE Journal of Selected Topics in Quantum Electronics*, vol. 17, no. 6, pp. 1552–1567, 2011.

[10] M. Müller, C. Grasse, and M. C. Amann, "InP-based 1.3 μm and 1.55 μm short-cavity VCSELs suitable for telecom- and datacom-applications," in *2012 14th International Conference on Transparent Optical Networks (ICTON)*, 2012, pp. 1–4.

[11] M. Grabherr, "New applications boost VCSEL quantities: recent developments at Philips," in *Vertical-Cavity Surface-Emitting Lasers XIX*, C. Lei and K. D. Choquette, Eds., vol. 9381, International Society for Optics and Photonics. SPIE, 2015, p. 938102.

[12] FindBiometrics. Apple Doubles Down On US VCSEL Supply Chain. (Accessed: 2022-08-11). [Online]. Available: https://findbiometrics.com/apple-doubles-down-us-vcsel-supply-chain-75202105/

[13] H. Moench, M. Carpaij, P. Gerlach, S. Gronenborn, R. Gudde, J. Hellmig, J. Kolb, and A. van der Lee, "VCSEL-based sensors for distance and velocity," in *Vertical-Cavity Surface-Emitting Lasers XX*, K. D. Choquette and J. K. Guenter, Eds., vol. 9766, International Society for Optics and Photonics. SPIE, 2016, p. 97660A.

[14] A. Einstein, *On the Quantum Theory of Radiation, CPAE, The collected papers of Albert Einstein*, J. Stachel et al., Ed. Princeton: Princeton University Press, 1987-2010, vol. 6, no. 38.

[15] J. T. Verdeyen, *Laser Electronics*, ser. Prentice Hall series in solid state physical electronics. Prentice-Hall International, 1995.

[16] B. E. Saleh and M. C. Teich, *Fundamentals of Photonics*. John Wiley & Sons, 2019.

[17] T. H. Maiman, "Stimulated optical radiation in ruby," *Nature*, vol. 187, pp. 493–494, 1960.

[18] M. A. Noginov, G. Zhu, A. M. Belgrave, R. Bakker, V. M. Shalaev, E. E. Narimanov, S. Stout, E. Herz, T. Suteewong, and U. Wiesner, "Demonstration of a spaser-based nanolaser," *Nature*, vol. 460, no. 7259, pp. 1110–1112, aug 2009.

[19] Lawrence Livermore National Laboratory. Building the World's Largest Laser. (Accessed: 2022-07-19). [Online]. Available: https://lasers.llnl.gov/10-years-of-dedication/building-nif

[20] A. White and J. Rigden, "Correspondence: Continuous gas maser operation in the visible," *Proceedings of the IRE*, vol. 50, no. 7, pp. 1683–1713, 1962.

[21] M. I. Nathan, W. P. Dumke, G. Burns, F. H. Dill, and G. Lasher, "Stimulated Emission of Radiation from GaAs p-n Junctions," *Applied Physics Letters*, vol. 1, no. 3, pp. 62–64, 1962.

[22] R. N. Hall, G. E. Fenner, J. D. Kingsley, T. J. Soltys, and R. O. Carlson, "Coherent light emission from gaas junctions," *Physical Review Letters*, vol. 9, pp. 366–368, Nov 1962.

[23] J. E. Geusic, H. M. Marcos, and L. G. Van Uitert, "Laser Oscillations in Nd-doped Yttrium Aluminum, Yttrium Gallium and Gadolinium Garnets," *Applied Physics Letters*, vol. 4, no. 10, pp. 182–184, 1964.

[24] K. Iga, "Vertical-Cavity Surface-Emitting Laser: Its Conception and Evolution," *Japanese Journal of Applied Physics*, vol. 47, no. 1, pp. 1–10, jan 2008.

[25] H. Soda, K. ichi Iga, C. Kitahara, and Y. Suematsu, "GaInAsP/InP Surface Emitting Injection Lasers," *Japanese Journal of Applied Physics*, vol. 18, no. 12, pp. 2329–2330, dec 1979.

[26] *IEICE Transactions*, no. 11, pp. 1089–1090, 1988.

[27] F. Koyama, S. Kinoshita, and K. Iga, "Room temperature continuous wave lasing characteristics of a GaAs vertical cavity surface emitting laser," *Applied Physics Letters*, vol. 55, no. 3, pp. 221–222, 1989.

[28] M. Grabherr, H. Moench, and A. Pruijmboom, *VCSELs for Optical Mice and Sensing*. Berlin, Heidelberg: Springer Berlin Heidelberg, 2013, pp. 521–538.

[29] Lumentum. VCSELs – Optics expertise for high-reliability, high-volume components. (Accessed: 2022-08-11). [Online]. Available: https://www.lumentum.com/en/diode-lasers/products/vcsels

[30] STMicroelectronics. STMicroelectronics' New Time-of-Flight Ranging Sensor Revolutionizes Mobile-Camera Performance and Unlocks New Applications in Robotics and IoT. (Accessed: 2022-08-11). [Online]. Available: https://www.st.com/content/st_com/en/about/media-center/press-item.html/p3775.html

[31] E. Simpanen, "Longer Wavelength GaAs-Based VCSELs for Extended-Reach Optical Interconnects," Ph.D. dissertation, Chalmers University of Technology, 2020.

[32] J. Lott, L. Buydens, K. Malloy, K. Kobayashi, and S. Ishikawa, "Visible (630-650 nm) vertical cavity surface emitting lasers with Al-oxide/AlGaInP/AlGaAs distributed Bragg reflectors," in *Compound Semiconductors 1995*. CRC Press, 1995, pp. 973–976.

[33] R. N. Hall, G. E. Fenner, J. D. Kingsley, T. J. Soltys, and R. O. Carlson, "Coherent Light Emission From GaAs Junctions," *Physical Review Letters*, vol. 9, pp. 366–368, Nov 1962.

[34] M. Jahed, J. S. Gustavsson, and A. Larsson, "Precise setting of micro-cavity resonance wavelength by dry etching," *Journal of Vacuum Science & Technology B*, vol. 37, no. 3, p. 031217, 2019.

[35] P. Westbergh, R. Safaisini, E. Haglund, J. S. Gustavsson, A. Larsson, and A. Joel, "High-speed 850-nm VCSELs with 28 GHz modulation bandwidth for short reach communication," in *Vertical-Cavity Surface-Emitting Lasers XVII*, K. D. Choquette and J. K. Guenter, Eds., vol. 8639, International Society for Optics and Photonics. SPIE, 2013, p. 86390X.

[36] D. Zhou and B. F. Usher, "Deviation of the AlGaAs lattice constant from Vegard's law," *Journal of Physics D: Applied Physics*, vol. 34, no. 10, pp. 1461–1465, may 2001.

[37] R. Michalzik, *VCSEL Fundamentals*. Berlin, Heidelberg: Springer Berlin Heidelberg, 2013.

[38] S. B. Healy, E. P. O'Reilly, J. S. Gustavsson, P. Westbergh, Å. Haglund, A. Larsson, and A. Joel, "Active Region Design for

High-Speed 850-nm VCSELs," *IEEE Journal of Quantum Electronics*, vol. 46, no. 4, pp. 506–512, 2010.

[39] W. Chow, K. Choquette, M. Crawford, K. Lear, and G. Hadley, "Design, Fabrication, and Performance of Infrared and Visible Vertical-Cavity Surface-Emitting Lasers," *IEEE Journal of Quantum Electronics*, vol. 33, no. 10, pp. 1810–1824, 1997.

[40] Y. Arakawa and A. Yariv, "Theory of Gain, Modulation Response, and Spectral Linewidth in AlGaAs Quantum Well Lasers," *IEEE Journal of Quantum Electronics*, vol. 21, no. 10, pp. 1666–1674, 1985.

[41] P. A. M. Dirac and N. H. D. Bohr, "The Quantum Theory of the Emission and Absorption of Radiation," *Proceedings of the Royal Society of London. Series A, Containing Papers of a Mathematical and Physical Character*, vol. 114, no. 767, pp. 243–265, 1927.

[42] L. A. Coldren, S. W. Corzine, and M. L. Mashanovitch, *Diode Lasers and Photonic Integrated Circuits*. John Wiley & Sons, 2012, vol. 218.

[43] J. L. Jewell, A. Scherer, S. L. McCall, Y. H. Lee, S. J. Walker, J. P. Harbison, and L. T. Florez, "Low-Threshold Electrically Pumps Vertical-Cavity Surface-Emitting Microlasers," *Optics News*, vol. 15, no. 12, pp. 10–11, Dec 1989.

[44] M. Orenstein, A. C. V. Lehmen, C. Chang-Hasnain, N. G. Stoffel, J. P. Harbison, L. T. Florez, E. Clausen, and J. E. Jewell, "Vertical-cavity surface-emitting InGaAs/GaAs lasers with planar lateral definition," *Applied Physics Letters*, vol. 56, no. 24, pp. 2384–2386, 1990.

[45] N. Dutta, L. Tu, G. Hasnain, G. Zydzik, Y. Wang, and A. Cho, "Anomalous temporal response of gain guided surface emitting lasers," *Electronics Letters*, vol. 27, no. 3, p. 208, 1991.

[46] D. L. Huffaker, D. G. Deppe, K. Kumar, and T. J. Rogers, "Native-oxide defined ring contact for low threshold vertical-cavity lasers," *Applied Physics Letters*, vol. 65, no. 1, pp. 97–99, 1994.

[47] B. Weigl, M. Grabherr, C. Jung, R. Jager, G. Reiner, R. Michalzik, D. Sowada, and K. Ebeling, "High-Performance Oxide-Confined

GaAs VCSELs," *IEEE Journal of Selected Topics in Quantum Electronics*, vol. 3, no. 2, pp. 409–415, 1997.

[48] W. Nakwaski, "Thermal aspects of efficient operation of vertical-cavity surface-emitting lasers," *Optical and Quantum Electronics*, vol. 28, no. 4, pp. 335–352, Apr. 1996.

[49] P. Westbergh, J. S. Gustavsson, Å. Haglund, M. Sköld, A. Joel, and A. Larsson, "High-Speed, Low-Current-Density 850 nm VCSELs," *IEEE Journal of Selected Topics in Quantum Electronics*, vol. 15, no. 3, pp. 694–703, 2009.

[50] L. W. Casperson, "Beam modes in complex lenslike media and resonators," *Journal of the Optical Society of America*, vol. 66, no. 12, pp. 1373–1379, Dec 1976.

[51] M. A. Bandres and J. C. Gutiérrez-Vega, "Ince–Gaussian beams," *Optics Letters*, vol. 29, no. 2, pp. 144–146, Jan 2004.

[52] Originally: Kes01, Used version: Alexander Grabowski. Laguerre-Gaussian modes. (Accessed: 2022-08-11). [Online]. Available: https://commons.wikimedia.org/wiki/File:Laguerre-Gaussian_modes.png

[53] SphereOptics. Integrating Sphere Design and Applications [PDF]. (Accessed: 2022-08-11). [Online]. Available: https://web.archive.org/web/20090815182409/http://www.sphereoptics.com/assets/sphere-optic-pdf/sphere-technical-guide.pdf

[54] E. Haglund, Å. Haglund, J. S. Gustavsson, B. Kögel, P. Westbergh, and A. Larsson, "Reducing the spectral width of high speed oxide confined VCSELs using an integrated mode filter," in *Vertical-Cavity Surface-Emitting Lasers XVI*, C. Lei and K. D. Choquette, Eds., vol. 8276, International Society for Optics and Photonics. SPIE, 2012, p. 82760L.

[55] J. Wang, M. V. R. Murty, C. Wang, D. Hui, A. L. Harren, H.-H. Chang, Z.-W. Feng, T. R. Fanning, A. Sridhara, S.-J. Taslim, X. Cai, J. Chu, and L. M. Giovane, "50Gb/s PAM-4 oxide VCSEL development progress at Broadcom," in *Vertical-Cavity Surface-Emitting Lasers XXI*, K. D. Choquette and C. Lei, Eds., vol. 10122, International Society for Optics and Photonics. SPIE, 2017, p. 1012202.

[56] J. Wang, M. V. R. Murty, Z.-W. Feng, S.-J. Taslim, A. Sridhara, X. Cai, A. L. Harren, N. Leong, G. H. Koh, A.-N. Cheng, D. W. Dolfi, J. Chu, and L. M. Giovane, "100Gb/s PAM4 oxide VCSEL development progress at Broadcom," in *Vertical-Cavity Surface-Emitting Lasers XXIV*, L. A. Graham and C. Lei, Eds., vol. 11300, International Society for Optics and Photonics. SPIE, 2020, p. 113000G.

[57] T. Lengyel, K. Szczerba, E. P. Haglund, P. Westbergh, M. Karlsson, A. Larsson, and P. A. Andrekson, "Impact of Damping on 50 Gbps 4-PAM Modulation of 25G Class VCSELs," *Journal of Lightwave Technology*, vol. 35, no. 19, pp. 4203–4209, 2017.

[58] Y. Satuby and M. Orenstein, "Mode-Coupling Effects on the Small-Signal Modulation of Multitransverse-Mode Vertical-Cavity Semiconductor Lasers," *IEEE Journal of Quantum Electronics*, vol. 35, no. 6, pp. 944–954, 1999.

[59] R. Nagarajan, M. Ishikawa, T. Fukushima, R. Geels, and J. Bowers, "Transport Limits in High Speed Quantum Well Lasers: Theory and Experiment," *IEEE Journal of Quantum Electronics*, vol. 28, p. 1990, 1992.

[60] R. Olshansky, P. Hill, V. Lanzisera, and W. Powazinik, "Frequency Response of 1.3 µm InGaAsP High Speed Semiconductor Lasers," *IEEE Journal of Quantum Electronics*, vol. 23, no. 9, pp. 1410–1418, 1987.

[61] N. Nishiyama, M. Arai, S. Shinada, K. Suzuki, F. Koyama, and K. Iga, "Multi-Oxide Layer Structure for Single-Mode Operation in Vertical-Cavity Surface-Emitting Lasers," *IEEE Photonics Technology Letters*, vol. 12, no. 6, pp. 606–608, 2000.

[62] E. O'Reilly and A. Adams, "Band-Structure Engineering in Strained Semiconductor Lasers," *IEEE Journal of Quantum Electronics*, vol. 30, no. 2, pp. 366–379, 1994.

[63] T. Lengyel, E. Simpanen, J. Gustavsson, A. Larsson, M. Karlsson, P. Andrekson, W. Sorin, S. Mathai, M. Tan, and S. Bickham, "Pre-emphasis enabled 50 Gbit/s transmission over 1000 m SMF using a 1060 nm single-mode VCSEL," *Electronics Letters*, vol. 54, no. 20, pp. 1186–1187, 2018.

[64] P. P. Baveja, B. Kögel, P. Westbergh, J. S. Gustavsson, Å. Haglund, D. N. Maywar, G. P. Agrawal, and A. Larsson, "Assessment of VCSEL thermal rollover mechanisms from measurements and empirical modeling," *Optics Express*, vol. 19, no. 16, pp. 15 490–15 505, Aug 2011.

[65] A. N. AL-Omari, A. Ababneh, and K. L. Lear, "High-Speed Inverted-Polarity Oxide-Confined Copper-Plated 850-nm Vertical-Cavity Lasers," *IEEE Journal of Selected Topics in Quantum Electronics*, vol. 21, no. 6, pp. 462–469, 2015.

[66] M. Müller, W. Hofmann, T. Gründl, M. Horn, P. Wolf, R. D. Nagel, E. Ronneberg, G. Bohm, D. Bimberg, and M.-C. Amann, "1550-nm High-Speed Short-Cavity VCSELs," *IEEE Journal of Selected Topics in Quantum Electronics*, vol. 17, no. 5, pp. 1158–1166, 2011.

[67] S. Adachi, "Lattice thermal resistivity of III–V compound alloys," *Journal of Applied Physics*, vol. 54, no. 4, pp. 1844–1848, 1983.

[68] Y. Ou, J. S. Gustavsson, P. Westbergh, A. Haglund, A. Larsson, and A. Joel, "Impedance Characteristics and Parasitic Speed Limitations of High-Speed 850-nm VCSELs," *IEEE Photonics Technology Letters*, vol. 21, no. 24, pp. 1840–1842, 2009.

[69] K. Szczerba, T. Lengyel, M. Karlsson, P. A. Andrekson, and A. Larsson, "94-Gb/s 4-PAM Using an 850-nm VCSEL, Pre-Emphasis, and Receiver Equalization," *IEEE Photonics Technology Letters*, vol. 28, no. 22, pp. 2519–2521, 2016.

[70] R. Nagarajan, M. Ishikawa, T. Fukushima, R. Geels, and J. Bowers, "High Speed Quantum-Well Lasers and Carrier Transport Effects," *IEEE Journal of Quantum Electronics*, vol. 28, no. 10, pp. 1990–2008, 1992.

[71] E. Kapon, *Semiconductor Lasers I: Fundamentals*. Academic Press, 1999.

[72] K. Osamura and Y. Murakami, "Free Carrier Absorption in n-GaAs," *Japanese Journal of Applied Physics*, vol. 11, no. 3, pp. 365–371, mar 1972.

[73] E. Haglund, P. Westbergh, J. S. Gustavsson, E. P. Haglund, and A. Larsson, "High-Speed VCSELs With Strong Confinement of Optical Fields and Carriers," *Journal of Lightwave Technology*, vol. 34, no. 2, pp. 269–277, Jan 2016.

[74] D. K. Serkland, G. A. Keeler, K. M. Geib, and G. M. Peake, "Narrow linewidth VCSELs for high-resolution spectroscopy," in *Vertical-Cavity Surface-Emitting Lasers XIII*, K. D. Choquette and C. Lei, Eds., vol. 7229, International Society for Optics and Photonics. SPIE, 2009, p. 722907.

[75] K. Petermann, *Laser Diode Modulation and Noise*. Springer Netherlands, 1988.

[76] J. Gustavsson, J. Bengtsson, and A. Larsson, "Spatially Dependent Noise Model for Vertical-Cavity Surface-Emitting Lasers," *IEEE Journal of Quantum Electronics*, vol. 40, no. 9, pp. 1163–1176, 2004.

[77] G. P. Agrawal, *Fiber-Optic Communication Systems*. John Wiley & Sons, 2012.

[78] P. Mena, J. Morikuni, S.-M. Kang, A. Harton, and K. Wyatt, "A Simple Rate-Equation-Based Thermal VCSEL Model," *Journal of Lightwave Technology*, vol. 17, no. 5, pp. 865–872, 1999.

[79] P. Mena, J. Morikuni, S.-M. Kang, A. Harton, and K. Wyatt, "A Comprehensive Circuit-Level Model of Vertical-Cavity Surface-Emitting Lasers," *Journal of Lightwave Technology*, vol. 17, no. 12, pp. 2612–2632, 1999.

[80] K. Szczerba and C. Kocot, "Behavioral modeling of VCSELs for high-speed optical interconnects," in *Vertical-Cavity Surface-Emitting Lasers XXII*, C. Lei and K. D. Choquette, Eds., vol. 10552, International Society for Optics and Photonics. SPIE, 2018, p. 1055204.

[81] S. Li, M. S. Nezami, D. Rolston, and O. Liboiron-Ladouceur, "A Compact High-Efficient Equivalent Circuit Model of Multi-Quantum-Well Vertical-Cavity Surface-Emitting Lasers for High-Speed Interconnects," *Applied Sciences*, vol. 10, no. 11, 2020.

[82] S. Li, M. S. Nezami, S. Mishra, and O. Liboiron-Ladouceur, "Spectral-dependent electronic-photonic modeling of high-speed vcsel-mmf links for optimized launch conditions," *Optics Express*, vol. 29, no. 2, pp. 2738–2756, Jan 2021.

[83] S. Li, M. S. Nezami, and O. Liboiron-Ladouceur, "Reach Extension in Short-Reach VCSEL-MMF Interconnects using a Coupling-Weighted Approach," in *2020 IEEE Photonics Conference (IPC)*, 2020, pp. 1–2.

[84] A. Melgar, V. Thomas, and S. E. Ralph, "Multimode VCSEL Parameter Extraction for Optical Link Models," in *2018 European Conference on Optical Communication (ECOC)*, 2018, pp. 1–3.

[85] A. Melgar, V. A. Thomas, B. D. Klein, I. Kalifa, P. Bakopoulos, E. Mentovich, and S. E. Ralph, "Behavioral PAM-4 VCSEL Model using Stochastic Multimode Rate Equations for Link Design Optimization," in *2022 Optical Fiber Communications Conference and Exhibition (OFC)*, 2022, pp. 1–3.

[86] B. Wang, W. V. Sorin, S. Palermo, and M. R. T. Tan, "Comprehensive vertical-cavity surface-emitting laser model for optical interconnect transceiver circuit design," *Optical Engineering*, vol. 55, no. 12, p. 126103, 2016.

[87] G. Belfiore, M. Khafaji, R. Henker, and F. Ellinger, "A Compact Electro-optical VCSEL Model for High-Speed IC Design," in *2016 12th Conference on Ph.D. Research in Microelectronics and Electronics (PRIME)*, 2016, pp. 1–4.

[88] M. Bruensteiner and G. Papen, "Extraction of VCSEL Rate-Equation Parameters for Low-Bias System Simulation," *IEEE Journal of Selected Topics in Quantum Electronics*, vol. 5, no. 3, pp. 487–494, 1999.

[89] C. Zhang, X. Liu, and C. P. Yue, "A Compact VCSEL Model for High-Speed Optical Interconnect Design," in *Laser Congress 2021 (ASSL,LAC)*. Optica Publishing Group, 2021, p. JTu1A.30.

[90] C. Liang, W. Zhang, Q. Wang, S. Yao, and Z. He, "Application-Oriented Investigation of Parasitic Limitation on Multilevel Modulation of High-Speed VCSELs," *IEEE Photonics Journal*, vol. 11, no. 3, pp. 1–10, 2019.

[91] C. Liang, W. Zhang, and Z. He, "Electro-Optical Co-Design of Power-Efficient 100-Gbps/λ VCSEL Transmitter," *IEEE Photonics Journal*, vol. 11, no. 6, pp. 1–11, 2019.

[92] J. Yan, J. Wang, C. Tang, X. Liu, G. Zhang, and Y. He, "An Electrooptothermal-Coupled Circuit-Level Model for VCSELs Under Pulsed Condition," *IEEE Transactions on Industrial Electronics*, vol. 66, no. 2, pp. 1315–1324, 2019.

[93] E. M. T. Fadaly, A. Dijkstra, J. R. Suckert, D. Ziss, M. A. J. van Tilburg, C. Mao, Y. Ren, V. T. van Lange, K. Korzun, S. Kölling, M. A. Verheijen, D. Busse, C. Rödl, J. Furthmüller, F. Bechstedt, J. Stangl, J. J. Finley, S. Botti, J. E. M. Haverkort, and E. P. A. M. Bakkers, "Direct-bandgap emission from hexagonal Ge and SiGe alloys," *Nature*, vol. 580, no. 7802, pp. 205–209, Apr. 2020.

[94] A. Z. Subramanian, P. Neutens, A. Dhakal, R. Jansen, T. Claes, X. Rottenberg, F. Peyskens, S. Selvaraja, P. Helin, B. Du Bois, K. Leyssens, S. Severi, P. Deshpande, R. Baets, and P. Van Dorpe, "Low-Loss Singlemode PECVD Silicon Nitride Photonic Wire Waveguides for 532–900 nm Wavelength Window Fabricated Within a CMOS Pilot Line," *IEEE Photonics Journal*, vol. 5, no. 6, pp. 2 202 809–2 202 809, 2013.

[95] D. Thomson, A. Zilkie, J. E. Bowers, T. Komljenovic, G. T. Reed, L. Vivien, D. Marris-Morini, E. Cassan, L. Virot, J.-M. Fédéli *et al.*, "Roadmap on silicon photonics," *Journal of Optics*, vol. 18, no. 7, p. 073003, 2016.

[96] S. S. Cheung and M. R. T. Tan, "Silicon Nitride (Si_3N_4) (De-)Multiplexers for 1-μm CWDM Optical Interconnects," *Journal of Lightwave Technology*, vol. 38, no. 13, pp. 3404–3413, Jul 2020.

[97] C. Doerr, J. Heanue, L. Chen, R. Aroca, S. Azemati, G. Ali, G. McBrien, L. Chen, B. Guan, H. Zhang, X. Zhang, T. Nielsen, H. Mezghani, M. Mihnev, C. Yung, and M. Xu, "Silicon Photonics Coherent Transceiver in a Ball-Grid Array Package," in *2017 Optical Fiber Communications Conference and Exhibition (OFC)*, 2017, pp. 1–3.

[98] G. Roelkens, A. Abassi, P. Cardile, U. Dave, A. De Groote, Y. De Koninck, S. Dhoore, X. Fu, A. Gassenq, N. Hattasan,

Q. Huang, S. Kumari, S. Keyvaninia, B. Kuyken, L. Li, P. Mechet, M. Muneeb, D. Sanchez, H. Shao, T. Spuesens, A. Z. Subramanian, S. Uvin, M. Tassaert, K. Van Gasse, J. Verbist, R. Wang, Z. Wang, J. Zhang, J. Van Campenhout, X. Yin, J. Bauwelinck, G. Morthier, R. Baets, and D. Van Thourhout, "III-V-on-Silicon Photonic Devices for Optical Communication and Sensing," *Photonics*, vol. 2, no. 3, pp. 969–1004, 2015.

[99] H. Lu, J. S. Lee, Y. Zhao, P. Cardile, A. Daly, L. Carroll, and P. O'Brien, "Hybrid integration of VCSELs onto a silicon photonic platform for biosensing application," in *Optical Diagnostics and Sensing XVII: Toward Point-of-Care Diagnostics*, G. L. Coté, Ed., vol. 10072, International Society for Optics and Photonics. SPIE, 2017, p. 100720K.

[100] A. Z. Subramanian, E. Ryckeboer, A. Dhakal, F. Peyskens, A. Malik, B. Kuyken, H. Zhao, S. Pathak, A. Ruocco, A. D. Groote, P. Wuytens, D. Martens, F. Leo, W. Xie, U. D. Dave, M. Muneeb, P. V. Dorpe, J. V. Campenhout, W. Bogaerts, P. Bienstman, N. L. Thomas, D. V. Thourhout, Z. Hens, G. Roelkens, and R. Baets, "Silicon and silicon nitride photonic circuits for spectroscopic sensing on-a-chip [Invited]," *Photonics Research*, vol. 3, no. 5, pp. B47–B59, Oct 2015.

[101] S. Koehl, A. Liu, and M. Paniccia, "Integrated Silicon Photonics: Harnessing the Data Explosion," *Optics and Photonics News*, vol. 22, no. 3, pp. 24–29, Mar 2011.

[102] Y. Shi, Z. Wang, J. V. Campenhout, M. Pantouvaki, W. Guo, B. Kunert, and D. V. Thourhout, "Optical pumped InGaAs/GaAs nano-ridge laser epitaxially grown on a standard 300-mm Si wafer," *Optica*, vol. 4, no. 12, pp. 1468–1473, Dec 2017.

[103] J. C. Norman, D. Jung, Z. Zhang, Y. Wan, S. Liu, C. Shang, R. W. Herrick, W. W. Chow, A. C. Gossard, and J. E. Bowers, "A Review of High-Performance Quantum Dot Lasers on Silicon," *IEEE Journal of Quantum Electronics*, vol. 55, no. 2, pp. 1–11, 2019.

[104] B. Stern, X. Ji, A. Dutt, and M. Lipson, "Compact narrow-linewidth integrated laser based on a low-loss silicon nitride ring

resonator," *Optics Letters*, vol. 42, no. 21, pp. 4541–4544, Nov 2017.

[105] E. Haglund, M. Jahed, J. S. Gustavsson, A. Larsson, J. Goyvaerts, R. Baets, G. Roelkens, M. Rensing, and P. O'Brien, "High-power single transverse and polarization mode VCSEL for silicon photonics integration," *Optics Express*, vol. 27, no. 13, pp. 18 892–18 899, Jun 2019.

[106] B. Snyder, B. Corbett, and P. O'Brien, "Hybrid Integration of the Wavelength-Tunable Laser With a Silicon Photonic Integrated Circuit," *Journal of Lightwave Technology*, vol. 31, no. 24, pp. 3934–3942, 2013.

[107] G. Roelkens, D. V. Thourhout, R. Baets, R. Nötzel, and M. Smit, "Laser emission and photodetection in an InP/InGaAsP layer integrated on and coupled to a Silicon-on-Insulator waveguide circuit," *Optics Express*, vol. 14, no. 18, pp. 8154–8159, Sep 2006.

[108] G. Roelkens, L. Liu, D. Liang, R. Jones, A. Fang, B. Koch, and J. Bowers, "III-V/silicon photonics for on-chip and intra-chip optical interconnects," *Laser & Photonics Reviews*, vol. 4, no. 6, pp. 751–779, 2010.

[109] E. P. Haglund, S. Kumari, P. Westbergh, J. S. Gustavsson, G. Roelkens, R. Baets, and A. Larsson, "Silicon-integrated short-wavelength hybrid-cavity VCSEL," *Optics Express*, vol. 23, no. 26, pp. 33 634–33 640, Dec 2015.

[110] A. W. Fang, H. Park, O. Cohen, R. Jones, M. J. Paniccia, and J. E. Bowers, "Electrically pumped hybrid AlGaInAs-silicon evanescent laser," *Optics Express*, vol. 14, no. 20, pp. 9203–9210, Oct 2006.

[111] S. Keyvaninia, M. Muneeb, S. Stanković, P. J. V. Veldhoven, D. V. Thourhout, and G. Roelkens, "Ultra-thin DVS-BCB adhesive bonding of III-V wafers, dies and multiple dies to a patterned silicon-on-insulator substrate," *Optical Materials Express*, vol. 3, no. 1, pp. 35–46, Jan 2013.

[112] M. Jahed, A. Caut, J. Goyvaerts, M. Rensing, M. Karlsson, A. Larsson, G. Roelkens, R. Baets, and P. O'Brien, "Angled Flip-Chip Integration of VCSELs on Silicon Photonic Integrated Cir-

cuits," *Journal of Lightwave Technology*, vol. 40, no. 15, pp. 5190–5200, 2022.

[113] S. Kumari, E. P. Haglund, J. S. Gustavsson, A. Larsson, G. Roelkens, and R. G. Baets, "Vertical-Cavity Silicon-Integrated Laser with In-Plane Waveguide Emission at 850 nm," *Laser & Photonics Reviews*, vol. 12, no. 2, p. 1700206, 2018.

[114] G. Roelkens, J. Zhang, A. De Groote, J. Juvert, N. Ye, S. Kumari, J. Goyvaerts, G. Muliuk, S. Uvin, G. Chen, B. Haq, B. Snyder, J. Van Campenhout, D. Van Thourhout, A. J. Trindade, C. Bower, J. O'Callaghan, R. Loi, B. Roycroft, and B. Corbett, "Transfer printing for silicon photonics transceivers and interposers," in *2018 IEEE Optical Interconnects Conference (OI)*, 2018, pp. 13–14.

[115] C. O. de Beeck, B. Haq, L. Elsinger, A. Gocalinska, E. Pelucchi, B. Corbett, G. Roelkens, and B. Kuyken, "Heterogeneous III-V on silicon nitride amplifiers and lasers via microtransfer printing," *Optica*, vol. 7, no. 5, pp. 386–393, May 2020.

[116] Chris Bower, X-Celeprint. (2014) Micro-Transfer-Printing (μTP): Technology Overview. (Accessed: 2022-09-13). [Online]. Available: http://site.ieee.org/ocs-cpmt/files/2013/06/CPMT_2014.02.11_V1_uTP.pdf

[117] M. A. Meitl, Z.-T. Zhu, V. Kumar, K. J. Lee, X. Feng, Y. Y. Huang, I. Adesida, R. G. Nuzzo, and J. A. Rogers, "Transfer printing by kinetic control of adhesion to an elastomeric stamp," *Nature Materials*, vol. 5, no. 1, pp. 33–38, Dec. 2005.

[118] A. Campbell Stephen, *Fabrication Engineering at the Micro- and Nanoscale (3rd Edition)*. Oxford University Press, 2008.

[119] K. Choquette, K. Geib, C. Ashby, R. Twesten, O. Blum, H. Hou, D. Follstaedt, B. Hammons, D. Mathes, and R. Hull, "Advances in Selective Wet Oxidation of AlGaAs Alloys," *IEEE Journal of Selected Topics in Quantum Electronics*, vol. 3, no. 3, pp. 916–926, 1997.

[120] J. Goyvaerts, "Near-Infrared GaAs-on-SiN Photonic Integration Platform Based on Micro-Transfer-Printing," Ph.D. dissertation, Ghent University, 2021.

[121] A. Rodríguez-Pérez, R. P. de Aranda, E. Prefasi, S. Dumont, J. Rosado, I. Enrique, P. Pinzón, and D. Ortiz, "Toward the Multi-Gigabit Ethernet for the Automotive Industry," *Fiber and Integrated Optics*, vol. 40, no. 1, pp. 1–13, 2021.

[122] C. Tabbert and C. Kuznia, "Chip Scale Package Fiber Optic Transceiver Integration for Harsh Environments," in *International Conference on Space Optics — ICSO 2014*, Z. Sodnik, B. Cugny, and N. Karafolas, Eds., vol. 10563, International Society for Optics and Photonics. SPIE, 2017, p. 1056335.